

**A HYBRID DISCONTINUOUS GALERKIN-MONTE
CARLO SIMULATOR FOR FILTERED DENSITY
FUNCTION**

by

Shervin Sammak

B.S. and M.S. in Aerospace Engineering, Tehran Polytechnic,
Tehran, 2011, 2013

M.S. in Petroleum Engineering, University of Pittsburgh,
Pittsburgh, 2016

Submitted to the Graduate Faculty of
the Swanson School of Engineering in partial fulfillment
of the requirements for the degree of

Doctor of Philosophy

University of Pittsburgh

2016

UNIVERSITY OF PITTSBURGH
SWANSON SCHOOL OF ENGINEERING

This dissertation was presented

by

Shervin Sammak

It was defended on

November 8, 2016

and approved by

Peyman Givi, Ph.D., Distinguished Professor, and James T. MacLeod Professor,

Department of Mechanical Engineering and Materials Science

John C. Brigham, Ph.D., Associate Professor, Department of Civil and Environmental

Engineering

William J. Layton, Ph.D., Professor, Department of Mathematics

Patrick Smolinski, Ph.D., Associate Professor, Department of Mechanical Engineering and

Material Science

Dissertation Director: Peyman Givi, Ph.D., Distinguished Professor, and James T.

MacLeod Professor, Department of Mechanical Engineering and Materials Science

Copyright © by Shervin Sammak
2016

A HYBRID DISCONTINUOUS GALERKIN-MONTE CARLO SIMULATOR FOR FILTERED DENSITY FUNCTION

Shervin Sammak, PhD

University of Pittsburgh, 2016

A new computational scheme is developed for large eddy simulation (LES) of compressible turbulent reacting flows via the filtered density function (FDF) subgrid scale closure. This is a hybrid scheme, combining the discontinuous Galerkin (DG) Eulerian solver with a Lagrangian Monte Carlo FDF simulator. The methodology is shown to be suitable for LES, as a larger portion of the resolved energy is captured as the order of spectral approximation increases. Simulations are conducted of both incompressible and compressible flows. The consistency and the overall performance of the DG-MC solver, and the realizability of the simulated results are demonstrated via LES of a temporally developing mixing layer under both non-reacting and reacting conditions. It is also shown that the scheme is capable of accurate simulation of shock dominated flows.

Keywords: Large eddy simulation; filtered density function; Monte Carlo methods; reacting flows; compressible turbulent flows.

TABLE OF CONTENTS

PREFACE	viii
1.0 INTRODUCTION	1
1.1 OBJECTIVE AND SCOPE	2
2.0 DG-MC FOR LES OF INCOMPRESSIBLE FLOW	4
2.1 FORMULATION	4
2.2 COUPLED DG-MC FDF SIMULATOR	7
2.3 RESULTS	9
3.0 DG-MC FOR LES OF COMPRESSIBLE FLOW	20
3.1 FORMULATION	20
3.2 RESULTS	24
4.0 CONCLUSION	35
BIBLIOGRAPHY	37

LIST OF FIGURES

1	(a) Ensemble averaging on unstructured mesh. (1): hexahedral with $\Delta_E = \Delta$. (2): hexahedral with $\Delta_E = \Delta/2$. (b) Schematic distribution of MC particles within a tetrahedral cell. The solid circles denote the MC particles and the solid squares denote the quadrature points.	8
2	Structured hexahedral mesh for the temporal mixing layer, and the distribution of Monte-Carlo particles within the domain at an initial time. The particles are colored by their scalar values.	10
3	Contour plots of the filtered scalar field for $p = 4$ at $t = 60$. (a) FDF, (b) DG.	12
4	Scatter plot of the filtered values as obtained by FDF vs. those obtained by DG for $p = 4$ at $t = 60$. (a) filtered scalar, the correlation coefficient is 0.9991. (b) SGS variance, the correlation coefficient is 0.9984.	12
5	Cross-stream variation of the Reynolds averaged values for $p = 2$ and various ensemble domain size. (a) filtered scalar field, (b) SGS scalar variance.	13
6	Cross-stream variation of the Reynolds-averaged values of the filtered scalar field for various degree of polynomial. (a) $p = 2$, (b) $p = 3$, (c) $p = 4$	14
7	Cross stream variation of the Reynolds averaged SGS scalar variance. The thick solid line denotes the DG data and dashed line denotes the FDF data. (a) $p = 2$, (b) $p = 3$, (c) $p = 4$	15
8	Cross-stream variation of the Reynolds-averaged values of the resolved scalar variance for various polynomial degree at $t = 60$. (a) $p = 2$, (b) $p = 3$, (c) $p = 4$.	16
9	Cross-stream variation of the Reynolds-averaged values of the total scalar vari- ance for various polynomial degree at $t = 60$. (a) $p = 2$, (b) $p = 3$, (c) $p = 4$. .	17

10	Scatter plots of the filtered composition variables versus the filtered mixture fraction for (a) $Da = 10^{-2}$, (b) $Da = 1$ and (c) $Da = 10^2$. The dashed lines denote pure mixing and infinitely fast chemistry limits.	18
11	Scatter plot of Z_2 vs. mixture fraction for $Da = 10^2$	19
12	Structured hexahedral mesh and distribution of Monte-Carlo particles within the domain at the initial time. The particles are colored by their scalar values.	25
13	Contour plots of the filtered scalar field for $p = 4$ and $M = 0.2$ at $t = 60$. (a) FDF, (b) DG.	26
14	Scatter plot of the filtered values as obtained by FDF vs. those obtained by DG for $p = 4$ and $M = 1.2$ at $t = 80$. (a) filtered scalar, the correlation coefficient is 0.9981. (b) filtered density, the correlation coefficient is 0.9871.	26
15	Cross-stream variation of the Reynolds averaged values for $p = 2$, $M = 0.2$ and various ensemble domain size. (a) filtered scalar field, (b) SGS scalar variance.	27
16	Contour plots of the filtered Mach number for the case with $Ma = 1.2$ at $t = 80$. (a) FDF, (b) DG.	29
17	Cross-stream variation of the filtered density at $t = 80$. (a) $Ma = 0.2$, (b) $Ma = 0.6$ and (c) $Ma = 1.2$	30
18	Vorticity thickness vs. time.	31
19	Cross stream variation of the Reynolds averaged SGS scalar variance at $t = 80$. (a) $Ma = 0.2$, (b) $Ma = 0.6$, (c) $Ma = 1.2$	32
20	Cross-stream variation of the Reynolds-averaged values of the resolved scalar variance at $t = 80$. (a) $Ma = 0.2$, (b) $Ma = 0.6$, (c) $Ma = 1.2$	33
21	Cross-stream variation of the Reynolds-averaged values of the total scalar variance at $t = 80$. (a) $Ma = 0.2$, (b) $Ma = 0.6$, (c) $Ma = 1.2$	34

PREFACE

I would like to express my sincere appreciation to my advisor, Professor Peyman Givi for his support and guidance through the course of my graduate studies. I would like to thank the members of my doctoral committee, Professors John Brigham, William Layton and Patrick Smolinski. Also, my appreciation goes to Professor Dimitri Mavriplis and Dr. Mike Brazell at University of Wyoming. It has been a pleasure to collaborate and interact with his group.

I am indebted to my colleagues and friends whom I had the pleasure to work with at one point or another during my time at the University of Pittsburgh: Mr. Cajon Gonzales, Mr. Mohammad Hashemi, Mr. Medet Inkarbekov, Ms. Wendy Janocha, Ms. Ling Miao, Dr. Mehdi Nik, Mr. Arash Nouri Gheimassi, Dr. Patrick Pisciuneri, Dr. Sasan Salkhordeh and Mr. Krisda Tapracharoen. My deepest gratitude goes to my parents, and my sister Shirin; for their love and support.

This work is sponsored by AFOSR under Grant FA9550-12-1-0057, and by NSF under Grant CBET-1609120 and Grant CBET-1603131. Computational resources are provided by the University of Pittsburgh Center for Research Computing.

SHERVIN SAMMAK

UNIVERSITY OF PITTSBURGH, 2016

1.0 INTRODUCTION

The filtered density function (FDF) is now widely recognized as a viable tool for large eddy simulation (LES) of turbulent flows [1–8]. It is also commonly believed that the Lagrangian Monte Carlo (MC) methods provide the most convenient means of solving the transported FDF equation [9, 10]. In MC, the physical domain is discretized in standard formats *e.g.* finite difference (FD), finite volume (FV), finite element (FE) or others; and the FDF is represented by an ensemble of *particles*. Each of these particles carry information pertaining to the physical field. For stable simulations, the MC solver must be coupled with an Eulerian base flow solver for the transport variables [11, 12]. The coupling must be done in such a way that the overall accuracy of the solver is maintained. It is also desired that the influence of the subgrid scale (SGS) quantities decrease with the increase of the resolution and/or the order of accuracy of the discretization procedure.

FDF in its initial form, the marginal “scalar” FDF (S-FDF); provided the first demonstration of a “transported” FDF in reacting flows. The primary advantage of S-FDF over conventional methods is that it accounts for the effects SGS chemical reactions in a closed form [13–15]. This is the most elementary form of FDF when it was first introduced, and has experienced widespread usage especially in combustion [16–25]. The most sophisticated FDF closure available to-date is pressure-velocity-scalar filtered mass density function and is due to Nouri *et al.* [26]. Some of the most noticeable contributions in FDF closure are in its basic implementation [27–33], and fine-tuning of numerical scheme [12, 34–36]. Despite its popularity, a major challenge associated with FDF is its implementation on higher order schemes. In all previous contributions, FDF is implemented on FD and FV. One of the advantages of higher order schemes over FD and FV is that, they result in very low numerical dissipation which is very desired (in fact essential) in LES.

In this work, we develop a hybrid algorithm that is suitable for simulating unsteady turbulent flows. For that, we use the discontinuous Galerkin (DG) method as the base flow solver. This method combines the versatility of FV discretization with the accuracy of spectral approximations and is shown here to be particularly suitable for coupling with the MC simulator. DG uses a basis that is continuous within an element but discontinuous between elements, and each element can have a different polynomial degree p for the solution and the geometrical mapping. The novelty of the new LES solver is that it supports curved mixed-element meshes, variable discretization order, and non-conforming mesh element refinement. These features enable the flow solver to support combined $h - p$ refinement which can result in optimal solution accuracy for a given computational cost [37, 38]. Based on the close to exponential convergence of p refinement, the procedure is much more efficient than the conventional approach of refining the grid (reducing h) as is the typical practice in typical Eulerian LES. These superior numerical efficiency of the DG method can be leveraged by using higher order polynomials.

1.1 OBJECTIVE AND SCOPE

The first object of the present work is to assess the capability of the DG-MC solver for LES of low Mach number flows. For that a three-dimensional temporally developing mixing layer under both non-reacting and reacting conditions is considered. The consistency of this solver is assessed by comparing the first two moments of the FDF with those obtained by the DG solutions of the same moments' transport equations. The overall predictive capability of the simulator is established via comparisons with previous direct numerical simulation (DNS) data [29, 30]. This is further demonstrated with comparing the profiles of the subgrid, resolved and total variance for different polynomial degrees. In the reacting case, the consistency of the FDF calculations and realizability of the simulated results are investigated by considering the compositional structure of the flame in the mixture fraction domain with relatively slow, moderate and relatively fast reaction rate.

The second objective of this work is to extend DG-MC to compressible flow simulations, and to conduct accurate LES of shock dominated flows. This is accomplished by considera-

tion of the energy equation and modeling the unclosed terms in a fashion similar to that in other scalars' equations. The consistency and the accuracy of this procedure are established by conducting LES of a compressible shear flow at different compressibility levels.

This dissertation is organized as follows. In Chapter 2, the hybrid DG-MC is developed for LES of incompressible flow. The work described in this chapter has been presented at APS-DFD and ICMIDS [39, 40]; and is published in *Computer and Fluids* [41]. In Chapter 3, the hybrid methodology is extended for LES of for variable density and compressible flows. This part of the work will be presented at AIAA-SciTech and APS-DFD [42, 43]. In Chapter 4, some final remarks are provided, along with some suggestions for future work. A part of this dissertation was the subject of an invited talk at the CITech 2015 Conference, and was subsequently published in an invited tutorial book chapter [44].

2.0 DG-MC FOR LES OF INCOMPRESSIBLE FLOW

In the work described in this chapter, a new computational methodology, termed “discontinuous Galerkin-Monte Carlo” (DG-MC), is developed for large eddy simulation (LES) of turbulent combustion via the filtered density function (FDF). This is a hybrid methodology which couples a Monte Carlo FDF simulator with a unstructured Eulerian LES solver. The consistency of the hybrid solver, and the realizability of the generated results are demonstrated via LES of a temporally developing mixing layer under both non-reacting and reacting condition.

2.1 FORMULATION

We start with the basic transport equations of a chemically reactive flow, involving N_s species. In this flow, the primary transport variables are the density $\rho(\mathbf{x}, t)$, the velocity vector $u_i(\mathbf{x}, t)$ ($i = 1, 2, 3$), the pressure $p(\mathbf{x}, t)$, the total specific enthalpy $h_s(\mathbf{x}, t)$, and the species mass fractions $Y_\alpha(\mathbf{x}, t)$ ($\alpha = 1, 2, \dots, N_s$). The equations which govern the transport of these variables in space (x_i) ($i = 1, 2, 3$) and time (t) are the continuity, momentum, conservation of enthalpy (energy) and species mass fraction equations, coupled with an equation of state. Large eddy simulation involves the spatial filtering operation [45, 46]:

$$\langle Q(\mathbf{x}, t) \rangle_\ell = \int_{-\infty}^{+\infty} Q(\mathbf{x}', t) G(\mathbf{x}', \mathbf{x}) d\mathbf{x}', \quad (2.1)$$

where $G(\mathbf{x}', \mathbf{x}) \equiv G(\mathbf{x}' - \mathbf{x})$ denotes a filter function, and $\langle Q(\mathbf{x}, t) \rangle_\ell$ is the filtered value of the transport variable $Q(\mathbf{x}, t)$. In variable-density flows it is convenient to use the Favré-

filtered quantity $\langle Q(\mathbf{x}, t) \rangle_L = \langle \rho Q \rangle_\ell / \langle \rho \rangle_\ell$. We consider a positive, physically varying filter function. We apply this function to the basic conservation transport equations:

$$\frac{\partial \langle \rho \rangle_\ell}{\partial t} + \frac{\partial \langle \rho \rangle_\ell \langle u_j \rangle_L}{\partial x_j} = 0, \quad (2.2)$$

$$\frac{\partial \langle \rho \rangle_\ell \langle u_i \rangle_L}{\partial t} + \frac{\partial \langle \rho \rangle_\ell \langle u_j \rangle_L \langle u_i \rangle_L}{\partial x_j} = -\frac{\partial \langle p \rangle_\ell}{\partial x_i} + \frac{\partial \langle \tau_{ij} \rangle_\ell}{\partial x_j} - \frac{\partial \Sigma_{ij}}{\partial x_j}, \quad (2.3)$$

$$\frac{\partial \langle \rho \rangle_\ell \langle \phi_\alpha \rangle_L}{\partial t} + \frac{\partial \langle \rho \rangle_\ell \langle u_j \rangle_L \langle \phi_\alpha \rangle_L}{\partial x_j} = -\frac{\partial \langle J_j^\alpha \rangle_\ell}{\partial x_j} - \frac{\partial M_j^\alpha}{\partial x_j} + \langle \rho S_\alpha \rangle_\ell. \quad (2.4)$$

Here, the viscous stress tensor and the scalar fluxes are represented by τ_{ij} and J_j^α , respectively. The chemical reaction source terms $S_\alpha \equiv S_\alpha(\boldsymbol{\phi}(\mathbf{x}, t))$ are functions of compositional scalars ($\boldsymbol{\phi} \equiv [\phi_1, \phi_2, \dots, \phi_{N_s+1}]$) where $\phi_\alpha \equiv Y_\alpha$, $\alpha = 1, 2, \dots, N_s$, and ϕ_{N_s+1} denotes the enthalpy. $\Sigma_{ij} = \langle \rho \rangle_\ell (\langle u_i u_j \rangle_L - \langle u_i \rangle_L \langle u_j \rangle_L)$ and $M_j^\alpha = \langle \rho \rangle_\ell (\langle u_j \phi_\alpha \rangle_L - \langle u_j \rangle_L \langle \phi_\alpha \rangle_L)$ denote the SGS stresses and the mass fluxes, respectively. For a Newtonian fluids obeying the Fick's law of diffusion and the Fourier's law of heat conduction, we have:

$$\tau_{ij} = \mu \left(\frac{\partial u_i}{\partial x_j} + \frac{\partial u_j}{\partial x_i} - \frac{2}{3} \frac{\partial u_k}{\partial x_k} \delta_{ij} \right), \quad J_j^\alpha = -\gamma \frac{\partial \phi_\alpha}{\partial x_j}, \quad (2.5)$$

where μ is the fluid dynamic viscosity, $\gamma = \mu/Sc$ denotes the thermal and mass molecular diffusivity coefficients for all the scalars, with Sc denoting the Schmidt/Lewis number. The FDF is considered for transport of all of the scalar quantities, and is denoted by F_L [8, 47]:

$$F_L(\boldsymbol{\psi}, \mathbf{x}, t) = \int_{-\infty}^{+\infty} \rho(\mathbf{x}', t) \zeta(\boldsymbol{\psi}, \boldsymbol{\phi}(\mathbf{x}', t)) G(\mathbf{x}' - \mathbf{x}) d\mathbf{x}', \quad (2.6)$$

where

$$\zeta(\boldsymbol{\psi}, \boldsymbol{\phi}(\mathbf{x}, t)) = \prod_{\alpha=1}^{\sigma} \delta(\psi_\alpha - \phi_\alpha(\mathbf{x}, t)). \quad (2.7)$$

Here, δ denotes the Dirac delta function, and $\boldsymbol{\psi}$ represents the scalar array in the sample space. The term ζ is the ‘‘fine-grained’’ density [48, 49], and Eq. (3.7) defines FDF as the spatially filtered value of the fine-grained density. With the condition of a positive filter

kernel [50], F_L has all the properties of a mass density function [49]. Defining the “conditional filtered value” of $Q(\mathbf{x}, t)$ as

$$\langle Q | \boldsymbol{\psi} \rangle_\ell \equiv \frac{\int_{-\infty}^{+\infty} Q(\mathbf{x}', t) \rho(\mathbf{x}', t) \zeta(\boldsymbol{\psi}, \boldsymbol{\phi}(\mathbf{x}', t)) G(\mathbf{x}' - \mathbf{x}) d\mathbf{x}'}{F_L(\boldsymbol{\psi}, \mathbf{x}, t)}, \quad (2.8)$$

the FDF is governed by the exact transport equation [7]:

$$\begin{aligned} \frac{\partial F_L}{\partial t} + \frac{\partial[\langle u_j(\mathbf{x}, t) | \boldsymbol{\psi} \rangle_\ell F_L]}{\partial x_j} &= -\frac{\partial}{\partial \psi_\alpha} [S_\alpha(\boldsymbol{\psi}) F_L] \\ &+ \frac{\partial}{\partial \psi_\alpha} \left[\left\langle \frac{1}{\rho(\boldsymbol{\phi})} \frac{\partial J_j^\alpha}{\partial x_j} \middle| \boldsymbol{\psi} \right\rangle_\ell F_L \right]. \end{aligned} \quad (2.9)$$

This equation indicates that the effect of chemical reaction (the first term on RHS) appears in a closed form. The unclosed nature of SGS convection and mixing is shown via the conditional filtered values in the other two terms. For closure of these terms, we use a gradient diffusion model for convection, and the linear mean square estimation (LMSE) model [13, 14] for the molecular mixing. These are given in terms of the stochastic differential equations (SDE's) [45, 48]:

$$dX_i^+(t) = \left[\langle u_i \rangle_L + \frac{1}{\langle \rho \rangle_\ell} \frac{\partial(\gamma + \gamma_t)}{\partial x_i} \right] dt + \sqrt{2(\gamma + \gamma_t) / \langle \rho \rangle_\ell} dW_i(t), \quad (2.10)$$

$$d\phi_\alpha^+ = -\Omega_m (\phi_\alpha^+ - \langle \phi_\alpha \rangle_L) dt + S_\alpha(\phi^+) dt, \quad (2.11)$$

where dW_i is the Wiener-Levy process [51] and, X_i^+ and ϕ_α^+ are probabilistic representations of the position and the scalar variables, respectively. In the model, $\Omega_m = C_\phi (\gamma + \gamma_t) / (\langle \rho \rangle_\ell \Delta^2)$ is the SGS mixing frequency and $C_\phi = 4$ is a model constant. The Fokker-Planck equation corresponding to this model is [52]:

$$\frac{\partial F_L}{\partial t} + \frac{\partial[\langle u_j \rangle_L F_L]}{\partial x_j} = \frac{\partial}{\partial x_j} \left[(\gamma + \gamma_t) \frac{\partial(F_L / \langle \rho \rangle_\ell)}{\partial x_j} \right] + \frac{\partial}{\partial \psi_\alpha} [\Omega_m (\psi_\alpha - \langle \phi_\alpha \rangle_L) F_L] - \frac{\partial[S_\alpha F_L]}{\partial \psi_\alpha}. \quad (2.12)$$

Equation (3.13) represents the modeled FDF transport equation. This equation may be integrated to obtain transport equations for the SGS moments. Since the FDF is involved

only for the scalar variable, all of the hydrodynamic SGS terms need to be modeled by other means. For those, we employ the standard Smagorinsky model [53, 54]:

$$\Sigma_{ij} - \frac{2}{3} \langle \rho \rangle_\ell C_{\nu_2} \Delta^2 S^2 \delta_{ij} = -2\mu_t \left(\langle S_{ij} \rangle_L - \frac{1}{3} \langle S_{kk} \rangle_L \delta_{ij} \right), \quad M_j^\alpha = -\gamma_t \frac{\partial \langle \phi_\alpha \rangle_L}{\partial x_j}. \quad (2.13)$$

The filtered strain rate tensor is $\langle S_{ij} \rangle_L = \frac{1}{2} \left[\frac{\partial \langle u_i \rangle_L}{\partial x_j} + \frac{\partial \langle u_j \rangle_L}{\partial x_i} \right]$. With that, the SGS viscosity is modeled by $\mu_t = \langle \rho \rangle_\ell [C_{\nu_1} \Delta]^2 S$, where $C_{\nu_1} = 0.2$, $C_{\nu_2} = 0.18$, $\gamma_t = \mu_t / Sc_t$, $Sc_t = 1$, $S = \sqrt{2 \langle S_{ij} \rangle_L \langle S_{ij} \rangle_L}$. The parameter Δ denotes the characteristic filter size and is taken as $\Delta = K_p \times (\Delta_x \Delta_y \Delta_z)^{\frac{1}{3}}$, where K_p estimated to be $\frac{1}{2(p+1)}$ with p denoting the polynomial order of approximation of the DG elements.

2.2 COUPLED DG-MC FDF SIMULATOR

The DG flow solver provides high-order approximations of the filtered transport equations with the flexibility to deal with complex geometries. To implement this solver, the domain is discretized into a number of structured or unstructured elements. Each of these elements are mapped from the physical space to the computational space ($\mathbf{x} \rightarrow \eta$). Within this space, the transport variable are represented via spectral approximations. The eigenfunctions of the appropriate Sturm-Liouville problem are used for this approximation. Here the Legendre polynomials are employed in conjunction with Gauss quadrature points [55]. The number of Gauss quadrature points is given by $ngp = p + 1$.

Unlike FE schemes, DG methods are discontinuous at the element interfaces, which makes them suitable for advection dominated problems. This property allows for flux calculation via approximate Riemann solvers as done here.

The FDF is represented by an ensemble of MC particles, each with a set of scalars $\phi_\alpha^n(t) = \phi_\alpha^n(X^{(n)}(t), t)$ and Lagrangian position vector $X^{(n)}$. This information is updated via temporal integration of the SDEs. By doing so, the position of the MC particles are updated due to convection and (random walk) diffusion; and their compositions are modified due to mixing and chemical reaction.

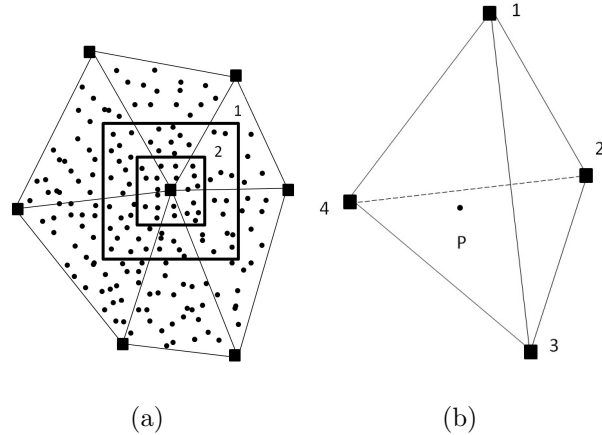


Figure 1: (a) Ensemble averaging on unstructured mesh. (1): hexahedral with $\Delta_E = \Delta$. (2): hexahedral with $\Delta_E = \Delta/2$. (b) Schematic distribution of MC particles within a tetrahedral cell. The solid circles denote the MC particles and the solid squares denote the quadrature points.

The DG-MC simulator as developed in this way has several advantages over more conventional methods (like FV, FD and FE). A significant advantage is that DG allows convergence to the DNS limit via p -refinement. Based on the close to exponential convergence of this refinement, the procedure is much more efficient than the conventional approaches of refining the grid (reducing h) as is the typical practice. Another advantage is that the DG variables can easily be evaluated at the MC particle's locations since these variables are represented by simple polynomials within each element. Hence, there is no loss of accuracy due to the use of a lower order interpolation method as is typically used in conventional approximations. Moreover, due to the high order polynomial approximation, the DG mesh elements are typically much larger than the cells in conventional discretizations. This implies that the FDF particles will remain much longer within one element as compared to those in conventional schemes, and thus the computational effort for the particle tracking algorithm is reduced significantly.

The MC statistics are constructed by consideration of an ensemble of N_p particles within a hexahedral domain of size Δ_E . This is illustrated in Fig. 2.2(a) for a domain discretized by

unstructured tetrahedral elements. For reliable statistics with minimal numerical dispersion, it is desired to minimize the size of the ensemble domain and maximize the number of the MC particles N_p . To maximize the statistical accuracy with finite number of particles, a variant of the basis function method is implemented [56].

Numerical solution of the SDEs (Eq. (3.11)) requires the input of the filtered velocity, the diffusion coefficient and gradients of the scalars field at the particle locations. These are provided by the DG solution, and subsequent evaluation at the particle locations. This procedure is called projection. Figure 2.2(b) provides a schematic of a tetrahedral cell showing its quadrature points with inclusion of the MC particle. Let 1, 2, 3, 4 denote the quadrature points. An estimate of the scalar values at the particle location (ϕ_p) is obtained by summing over all polynomial degrees in the linked element and taking into account the Legendre basis functions:

$$\phi_p = \sum_{j=1}^{ngp} \phi_j \mathcal{L}_j(p), \quad (2.14)$$

Similar to that observed in other hybrid approaches, with this coupled DG-MC algorithm, several of the transport variables are calculated repeatedly [4]. This “redundancy” is very important to establish consistency as will be demonstrated below.

2.3 RESULTS

Simulations are conducted on a three-dimensional, temporally developing mixing layer, similar to those in previous DNS [29, 50]. The layer consists of two parallel streams traveling in opposite directions with the same speed. In the representation below, x , y and z denote the stream-wise, the cross-stream and the span-wise flow directions respectively (Fig. 12). The velocity components in these directions are denoted by u , v and w . The filtered stream-wise velocity is initialized with a hyperbolic tangent profile with $\langle u \rangle_L = 1$ on the top stream and $\langle u \rangle_L = -1$ on the bottom stream. All of the Reynolds-averaged values are time-dependent and are determined by ensemble averaging over the homogeneous $x - z$ planes. These are denoted by an overbar.

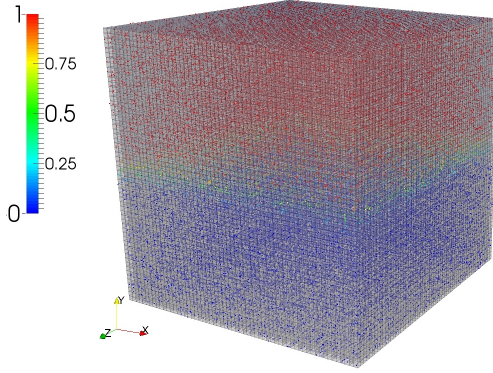


Figure 2: Structured hexahedral mesh for the temporal mixing layer, and the distribution of Monte-Carlo particles within the domain at an initial time. The particles are colored by their scalar values.

The simulations are conducted on a cube box, $0 \leq x \leq L, -L/2 \leq y \leq L/2$ and $0 \leq z \leq L$. The box length L is specified such that $L = 2^{n_p} \lambda_u$, where n_p is the desired number of successive vortex pairings and λ_u is the wavelength of the most unstable mode corresponding to the mean stream-wise velocity profile imposed at the initial time. The flow variables are normalized with respect to the half initial vorticity thickness, $L_r = [\delta_v(t=0)/2]$; $\delta_v = \Delta U / |\partial \overline{\langle u \rangle} / \partial y|_{max}$, where $\overline{\langle u \rangle}$ is the Reynolds averaged value of the filtered stream-wise velocity and ΔU is the velocity difference across the layer. The reference velocity is $U_r = \Delta U / 2$. The Reynolds number based on the reference velocity and length scales is $Re = 50$. The formation of the large scale vortical structures are expedited by harmonic forcing of the layer. This includes 2D and 3D perturbations with a random phase shift between the 3D modes [50]. This results in the formation of two successive vortex pairings and strong three dimensionality caused by growth of secondary instabilities.

Both non-reacting and reacting layers are considered. In the former, the trace of a passive scalar ϕ is considered. This is again initialized as a hyperbolic tangent profile with $\langle \phi \rangle_L = 1$ and 0 on the top and bottom streams, respectively. In the reacting case, an irreversible,

second-order reaction scheme of type $\mathcal{A} + \nu\mathcal{B} \rightarrow (\nu + 1)\mathcal{P}$ is considered. The reactant conversion is governed by $S_A = -k_r AB$, where k_r is the reaction rate constant; and A , B denote the mass fractions of the two reactants. In this case, the reactants are initialized such that $A \equiv \phi$ (as described above), and $B = 1 - A$. The stoichiometric coefficient is unity. The temperature in both streams is kept constant at $T = T_\infty$, and the combustion exothermicity ($-\Delta H$) is parameterized via the heat release parameter $\mathcal{Q} = \frac{-\Delta H}{C_p T_\infty} = 0.1$, where C_p denotes the specific heat value at constant pressure. The rate of reactant conversion is parameterized by the Damköhler number, $Da = k_r L_r / U_r$. Simulations are conducted with relatively slow ($Da = 10^{-2}$), moderate ($Da = 1$) and relatively fast ($Da = 10^2$) reactions.

To establish the consistency and convergence of the MC solver, the generalized first SGS moment $\langle \phi_\alpha \rangle_L$ and the SGS variance $\tau_\alpha \equiv \tau(\phi_\alpha, \phi_\alpha)$ are considered. These moments are obtained via integration of the modeled FDF transport equation (Eq. (3.13)), as given by:

$$\frac{\partial(\langle \rho \rangle_\ell \langle \phi_\alpha \rangle_L)}{\partial t} + \frac{\partial[\langle \rho \rangle_\ell \langle u_j \rangle_L \langle \phi_\alpha \rangle_L]}{\partial x_j} = \frac{\partial}{\partial x_j} \left[(\gamma + \gamma_t) \frac{\partial(\langle \phi_\alpha \rangle_L)}{\partial x_j} \right] + \langle \rho \rangle_\ell \langle S_\alpha \rangle_L, \quad (2.15)$$

$$\begin{aligned} \frac{\partial(\langle \rho \rangle_\ell \tau_\alpha)}{\partial t} + \frac{\partial[\langle \rho \rangle_\ell \langle u_j \rangle_L \tau_\alpha]}{\partial x_j} &= \frac{\partial}{\partial x_j} \left[(\gamma + \gamma_t) \frac{\partial \tau_\alpha}{\partial x_j} \right] + 2(\gamma + \gamma_t) \left[\frac{\partial(\langle \phi_\alpha \rangle_L)}{\partial x_j} \frac{\partial(\langle \phi_\alpha \rangle_L)}{\partial x_j} \right] \\ &- 2\Omega_m \langle \rho \rangle_\ell \tau_\alpha + 2 \langle \rho \rangle_\ell (\langle \phi_\alpha S_\alpha \rangle_L - \langle \phi_\alpha \rangle_L \langle S_\alpha \rangle_L). \end{aligned} \quad (2.16)$$

These equations are identical to those which would be obtained by employing consistent closures for the SGS fluxes and the dissipation from Eq. (3.4). In such a direct moment formulation, however, the terms involving $\langle S_\alpha \rangle_L$ require modeling.

The DG-MC FDF simulator is invoked in conjunction with Lax-Friedrichs [57], Roe [58] and artificially upstream flux vector splitting scheme [59] for the advective fluxes, and a symmetric interior penalty method [60, 61] for the diffusive fluxes. Temporal integration in the DG calculations is via a 4th order Runge Kutta method [62]. The SDEs in the MC solver are integrated via the Euler-Marruyamma approximation [9]. The computational domain is discretized on equally spaced cells. These points are used for two purposes: (1) to identify the regions where the statistical information from the MC simulations is obtained; (2) to assess consistency of the coupled DG-MC solver (as described below). Simulations are conducted on a structured hexahedral mesh with a total number of cells equal to 35,937. The MC

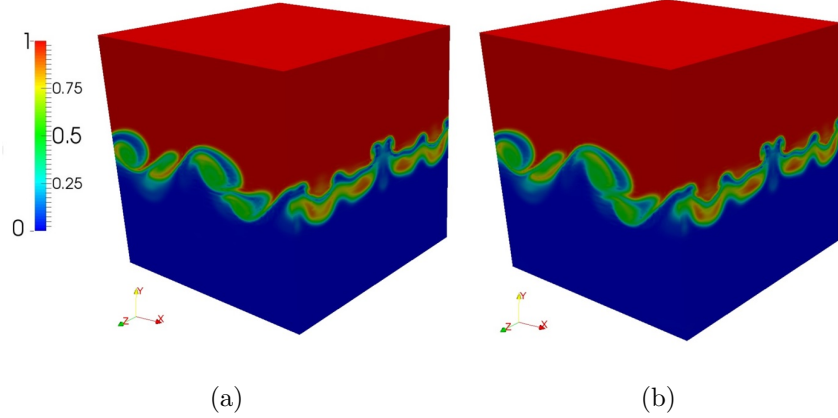


Figure 3: Contour plots of the filtered scalar field for $p = 4$ at $t = 60$. (a) FDF, (b) DG.

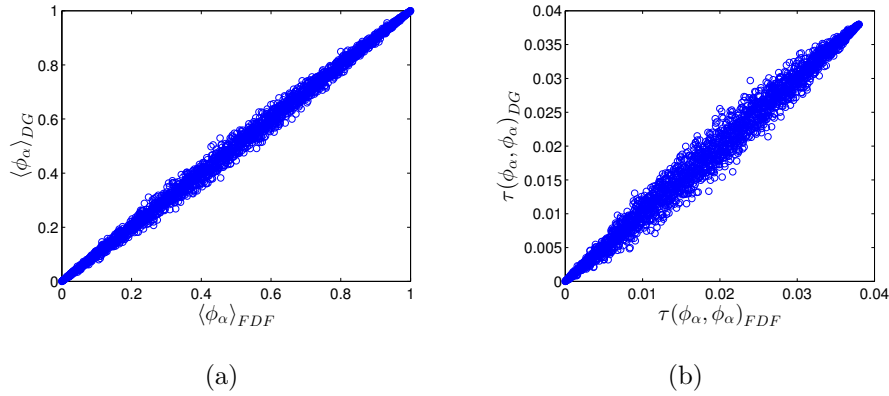


Figure 4: Scatter plot of the filtered values as obtained by FDF vs. those obtained by DG for $p = 4$ at $t = 60$. (a) filtered scalar, the correlation coefficient is 0.9991. (b) SGS variance, the correlation coefficient is 0.9984.

particles are initially distributed somewhat uniformly throughout the domain. The initial number of particles per cell is 40. Figure 12 shows the distribution of MC particles inside the cube with the structured mesh at an initial time. The simulated results are analyzed both instantaneously and statistically. In the former, the snap-shot contours and scatter plots of the scalar variable are displayed. In the latter, the Reynolds averaged values are considered. In the presentation below, $\tau(a, b) = \langle ab \rangle_L - \langle a \rangle_L \langle b \rangle_L$ denotes the SGS stresses. The resolved

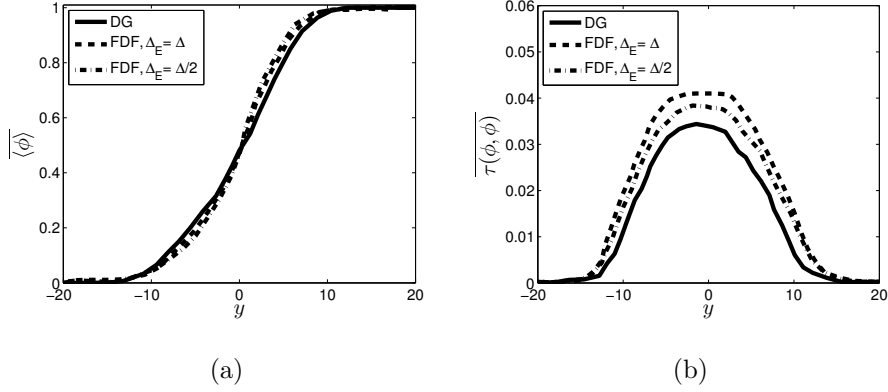


Figure 5: Cross-stream variation of the Reynolds averaged values for $p = 2$ and various ensemble domain size. (a) filtered scalar field, (b) SGS scalar variance.

stresses are expressed by $R(a, b) = \overline{\langle a \rangle_L \langle b \rangle_L} - \left(\overline{\langle a \rangle_L} \right) \left(\overline{\langle b \rangle_L} \right)$ and the total stresses are given by $r(a, b) = \overline{\langle ab \rangle} - \overline{a} \overline{b}$. Note that for a generic filter, $r(a, b) = R(a, b) + \overline{\tau(a, b)}$.

The overall consistency of the simulator is best achieved by comparing the lower moments as obtained from FDF with those simulated directly via DG on the same mesh. The chemical source terms are evaluated solely via the MC and are then used in the DG solution of the filtered scalar equations. In this way, the filtered scalar values are obtained via both DG and MC. Figure 13 shows the instantaneous contour plots of filtered scalar ($\langle \phi_\alpha \rangle_L$) field as computed via both DG and MC. This figure provides a visual demonstration of the consistency of the FDF simulation as the MC results are in agreement with those via DG. This is corroborated quantitatively by the scatter plots of the instantaneous filtered values in Fig. 14.

Figure 15 shows the influence of Δ_E in both filtered scalar ($\langle \phi_\alpha \rangle_L$) field and the SGS variance $\tau(\phi, \phi)$. It is indicated that, the size of the ensemble domain does not have a significant influence on the Reynolds statistics of the first filtered moments. However, for the SGS variance, the FDF and the DG solutions merge as the size of the ensemble domain decreases. The best agreement is observed with a ensemble domain size $\Delta_E = \Delta/2$. Hereinafter, unless otherwise noted, statistics are generated with consideration of $\Delta_E = \Delta/2$.

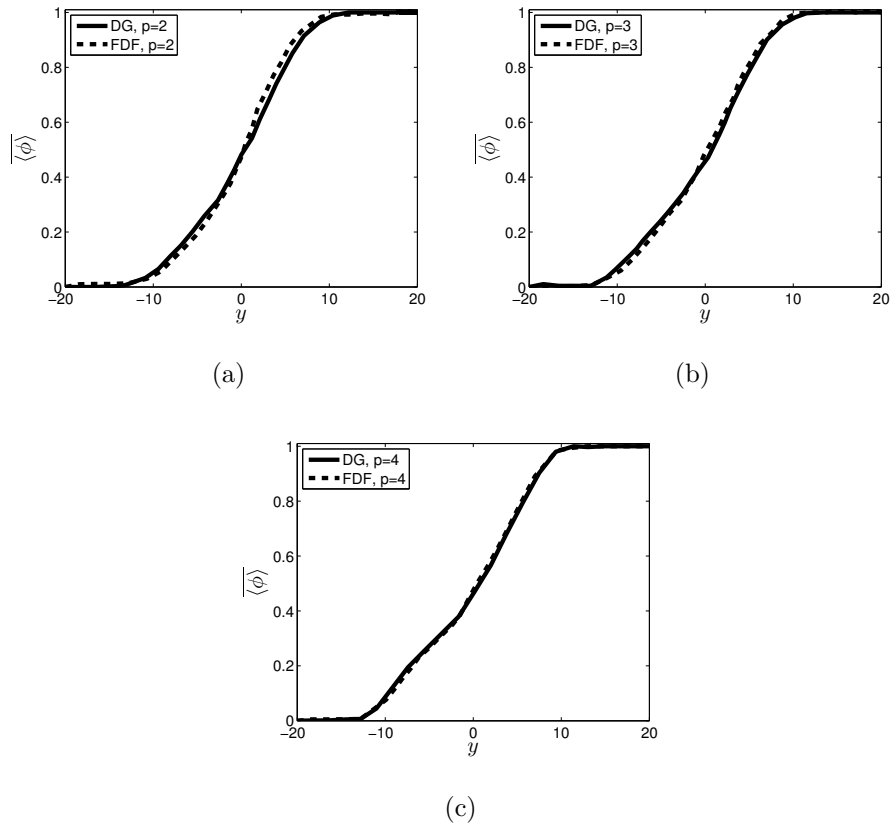


Figure 6: Cross-stream variation of the Reynolds-averaged values of the filtered scalar field for various degree of polynomial. (a) $p = 2$, (b) $p = 3$, (c) $p = 4$.

In Fig. 6 the first order moment from MC solver compared to those obtained by the DG for various polynomial degrees. Since the accuracy of the DG procedure is well-established (at least for the first-order filtered quantities), such a consistency assessment provides a good means of assessing the performance of the MC solution. As shown (and somewhat expected), the first filtered values are not significantly influenced by the larger values of p . However, this is not the case for the variances as shown in Fig. 19. It is clear that as the value of p increases, the amount of SGS energy decreases. This is in accord with the expectation that with increased resolution, the influence of SGS scales becomes less pronounced. This is further demonstrated in Fig. 20 in which the profiles of the resolved variances are shown. Consistent with the philosophy of LES, as the solution becomes more

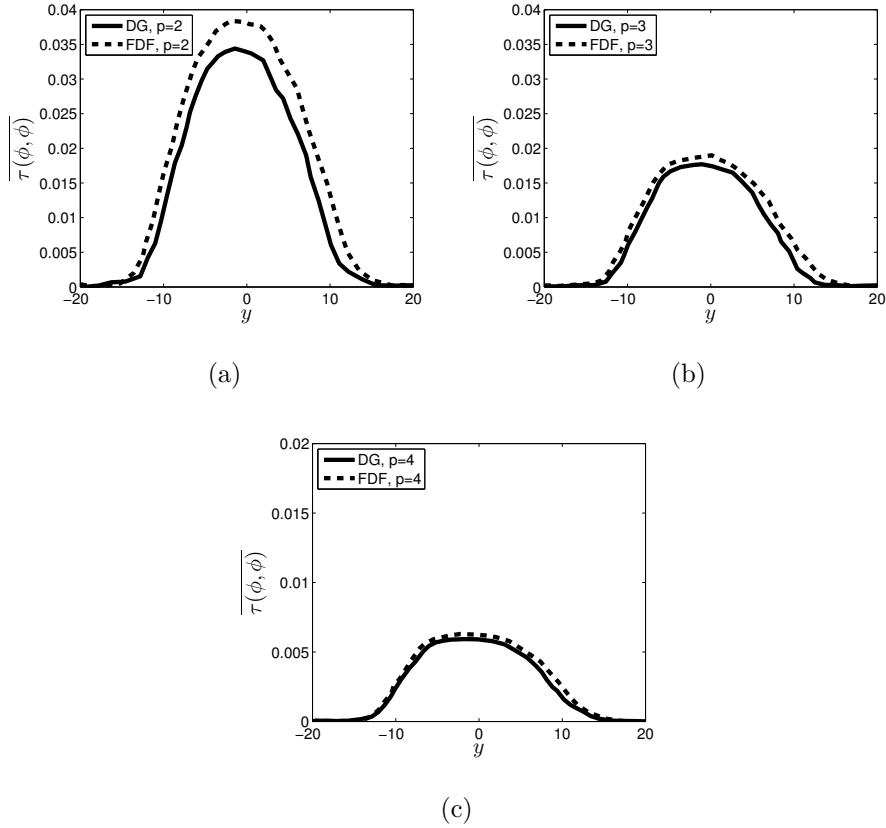


Figure 7: Cross stream variation of the Reynolds averaged SGS scalar variance. The thick solid line denotes the DG data and dashed line denotes the FDF data. (a) $p = 2$, (b) $p = 3$, (c) $p = 4$.

accurate, a more significant portion of the energy is resolved. In all cases, the total energy remains the same, as shown in Fig. 21. For all p values, the LES predictions are in close agreements with DNS data. This is very encouraging as it indicates that regardless of the portion of energy captured by the resolved field, the total energy is predicted well and there is no contamination of the total field due to SGS modeling.

In the reacting case, the consistency of the FDF calculations and realizability of the simulated results are investigated by considering the compositional structure of the flame in the mixture fraction domain ξ [63]. As shown in Fig. 10, when chemistry is slow the composition is close to that of pure mixing. On the opposite side of the spectrum, for very

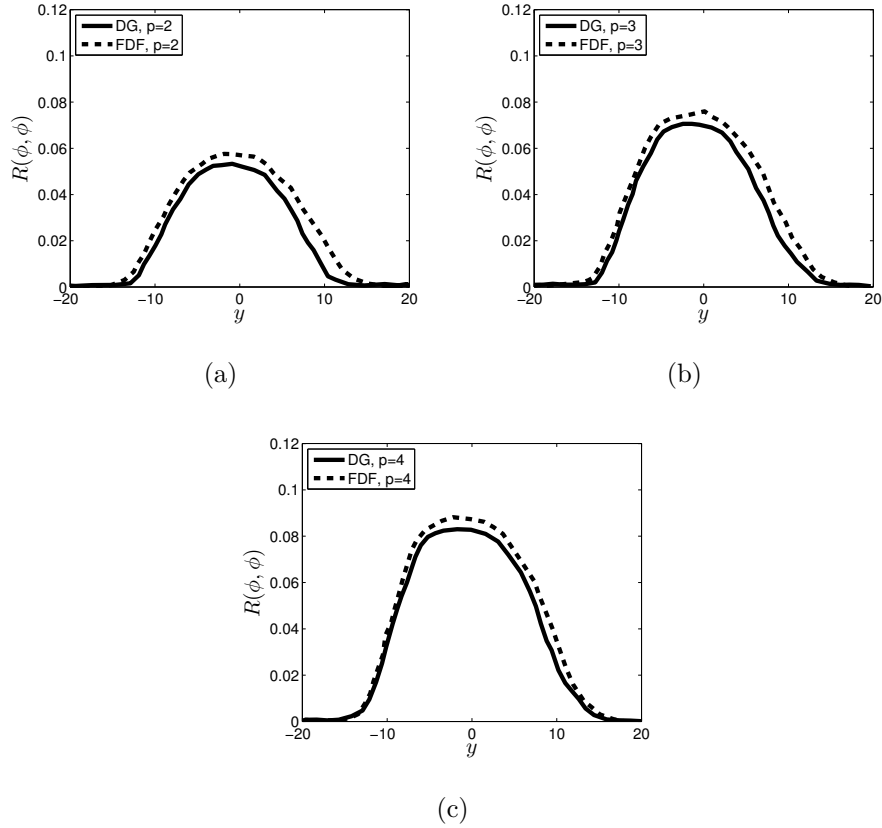


Figure 8: Cross-stream variation of the Reynolds-averaged values of the resolved scalar variance for various polynomial degree at $t = 60$. (a) $p = 2$, (b) $p = 3$, (c) $p = 4$.

fast reactions, the composition is close to that of the infinitely fast reaction. For the moderate chemistry, the compositional structure is similar to that of a distributed reaction zone. To demonstrate accuracy, transport of two Shvab-Zeldovich variables [64] are also considered:

$$Z_1 = \frac{A - \frac{B}{\nu} + \frac{B_\infty}{\nu}}{A_\infty + \frac{B_\infty}{\nu}}, \quad (2.17)$$

where the subscript ∞ denotes the values at the free streams. Figure 11 demonstrates that the conserved scalar and the mixture fraction are nearly perfectly correlated for $Da = 10^2$. The results for the other two cases are, as expected, very similar and thus are not presented.

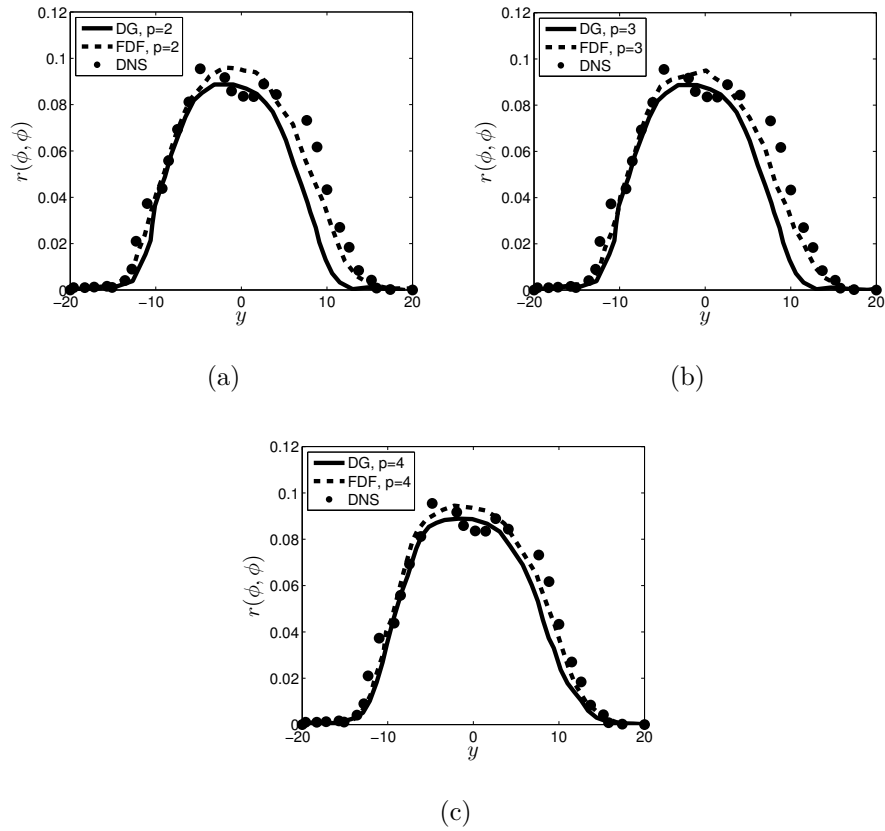


Figure 9: Cross-stream variation of the Reynolds-averaged values of the total scalar variance for various polynomial degree at $t = 60$. (a) $p = 2$, (b) $p = 3$, (c) $p = 4$.

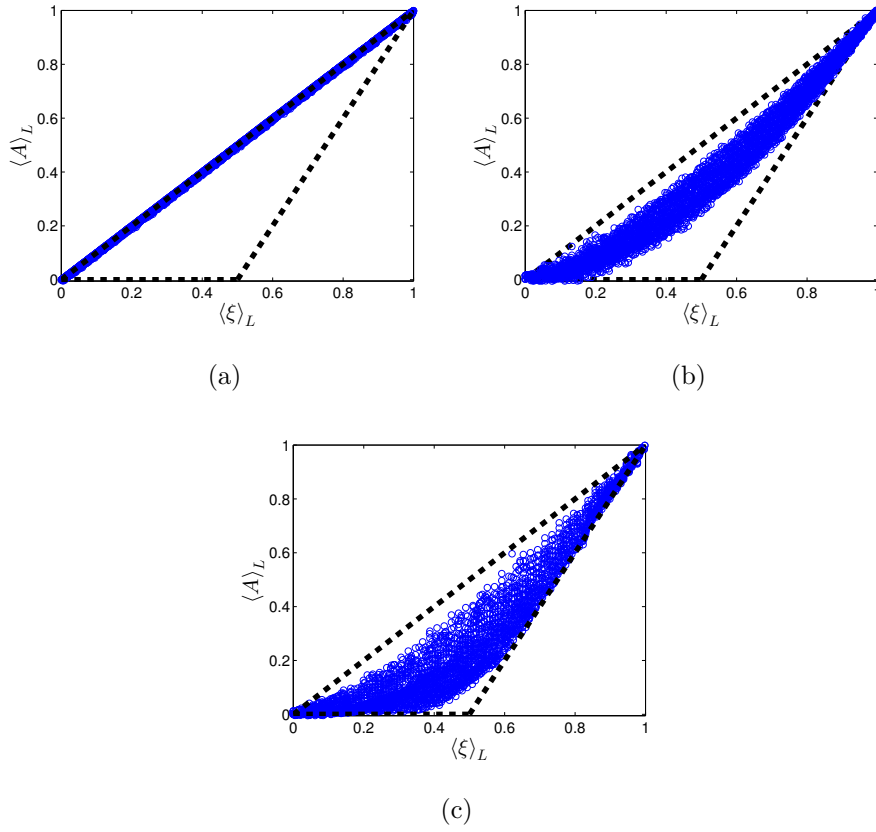


Figure 10: Scatter plots of the filtered composition variables versus the filtered mixture fraction for (a) $Da = 10^{-2}$, (b) $Da = 1$ and (c) $Da = 10^2$. The dashed lines denote pure mixing and infinitely fast chemistry limits.

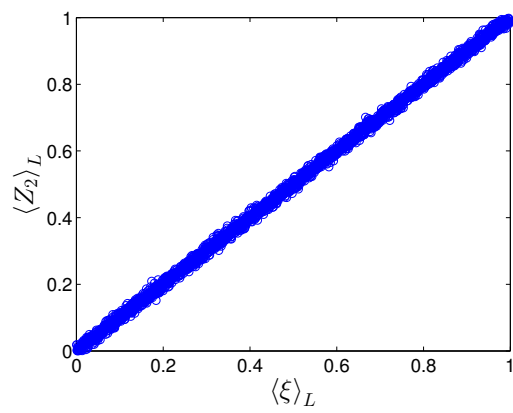


Figure 11: Scatter plot of Z_2 vs. mixture fraction for $Da = 10^2$.

3.0 DG-MC FOR LES OF COMPRESSIBLE FLOW

In the work described in this chapter, the DG-MC methodology is extended for LES of compressible turbulent flows. This is achieved by considering the energy equation and modeling the unclosed terms in a fashion similar to that in the other scalars' equations. The consistency and the accuracy of this procedure are established by conducting LES of a three dimensional, temporally evolving mixing layer involving the transport of a passive scalar. Simulations are conducted at several compressibility levels.

3.1 FORMULATION

In a compressible reacting flows, the primary transport variables are the density $\rho(\mathbf{x}, t)$, the velocity vector $u_i(\mathbf{x}, t)$ ($i = 1, 2, 3$), the pressure $p(\mathbf{x}, t)$, the internal energy $E(\mathbf{x}, t)$, and the species mass fractions $Y_\alpha(\mathbf{x}, t)$ ($\alpha = 1, 2, \dots, N_s$). The conservation equations governing these variables are the continuity; conservation of momentum, internal energy and species mass fractions; along with an equation of state [65]. Large eddy simulation involves the use of spatial filtering operation [45, 46, 66, 67]:

$$\langle Q(\mathbf{x}, t) \rangle_\ell = \int_{-\infty}^{+\infty} Q(\mathbf{x}', t) G(\mathbf{x}', \mathbf{x}) d\mathbf{x}', \quad (3.1)$$

where G denotes a filter function, and $\langle Q(\mathbf{x}, t) \rangle_\ell$ represents the filtered value of the transport variable $Q(\mathbf{x}, t)$ is the filtered value of the transport variable $Q(\mathbf{x}, t)$. In variable-density flows it is convenient to use the Favré-filtered quantity $\langle Q(\mathbf{x}, t) \rangle_L = \langle \rho Q \rangle_\ell / \langle \rho \rangle_\ell$. We consider a positive, spatially and temporally invariant filter functions, thus $G(\mathbf{x}', \mathbf{x}) \equiv G(\mathbf{x}' - \mathbf{x})$

with $G(\mathbf{x}) = G(-\mathbf{x})$ and $\int_{-\infty}^{\infty} G(\mathbf{x})d(\mathbf{x}) = 1$. Applying the filtering operation to the basic conservation transport equations fields [67]:

$$\frac{\partial \langle \rho \rangle_{\ell}}{\partial t} + \frac{\partial \langle \rho \rangle_{\ell} \langle u_j \rangle_L}{\partial x_j} = 0, \quad (3.2)$$

$$\frac{\partial \langle \rho \rangle_{\ell} \langle u_i \rangle_L}{\partial t} + \frac{\partial \langle \rho \rangle_{\ell} \langle u_j \rangle_L \langle u_i \rangle_L}{\partial x_j} = -\frac{\partial \langle p \rangle_{\ell}}{\partial x_i} + \frac{\partial \langle \tau_{ij} \rangle_{\ell}}{\partial x_j} - \frac{\partial \Sigma_{ij}}{\partial x_j}, \quad (3.3)$$

$$\frac{\partial \langle \rho \rangle_{\ell} \langle \phi_{\alpha} \rangle_L}{\partial t} + \frac{\partial \langle \rho \rangle_{\ell} \langle u_j \rangle_L \langle \phi_{\alpha} \rangle_L}{\partial x_j} = -\frac{\partial \langle J_j^{\alpha} \rangle_{\ell}}{\partial x_j} - \frac{\partial M_j^{\alpha}}{\partial x_j} + \langle \rho S_{\alpha} \rangle_{\ell}, \quad (3.4)$$

$$\begin{aligned} \frac{\partial \langle \rho \rangle_{\ell} \langle E \rangle_L}{\partial t} + \frac{\partial \langle \rho \rangle_{\ell} \langle u_j \rangle_L \langle E \rangle_L}{\partial x_j} &= -\frac{\partial \langle q_j \rangle_{\ell}}{\partial x_j} - \frac{\partial \langle p \rangle_{\ell} \langle u_j \rangle_L}{\partial x_j} + \frac{\partial \langle u_i \rangle_L \langle \tau_{ij} \rangle_{\ell}}{\partial x_j} \\ &- \frac{\partial \mathcal{E}_j}{\partial x_j} + \frac{\partial \mathcal{V}_j}{\partial x_j} - \frac{\partial \mathcal{T}_j}{\partial x_j}. \end{aligned} \quad (3.5)$$

Here, the viscous stress tensor and the scalar fluxes are represented by τ_{ij} and J_j^{α} , respectively. The chemical reaction source terms $S_{\alpha} \equiv S_{\alpha}(\phi(\mathbf{x}, t))$ are functions of compositional scalars ($\phi \equiv [\phi_1, \phi_2, \dots, \phi_{N_s}]$) where $\phi_{\alpha} \equiv Y_{\alpha}, \alpha = 1, 2, \dots, N_s$. The terms $\Sigma_{ij} = \langle \rho \rangle_{\ell} (\langle u_i u_j \rangle_L - \langle u_i \rangle_L \langle u_j \rangle_L)$ and $M_j^{\alpha} = \langle \rho \rangle_{\ell} (\langle u_j \phi_{\alpha} \rangle_L - \langle u_j \rangle_L \langle \phi_{\alpha} \rangle_L)$ denote the SGS stresses and the mass fluxes, respectively. The unclosed terms in internal energy equation are the SGS energy flux, $\mathcal{E}_j = \langle \rho \rangle_{\ell} (\langle u_j E \rangle_L - \langle u_j \rangle_L \langle E \rangle_L)$, SGS viscous dissipation, $\mathcal{V}_j = (\langle u_j \tau_{ij} \rangle_{\ell} - \langle u_j \rangle_L \langle \tau_{ij} \rangle_{\ell})$, and SGS convected pressure, $\mathcal{T}_j = (\langle u_j p \rangle_{\ell} - \langle u_j \rangle_L \langle p \rangle_{\ell})$.

Assuming a Newtonian fluids with Fick's law of diffusion and Fourier's law of heat conduction, the viscous stress tensor τ_{ij} , the mass flux J_j^{α} , and the heat flux q_j are represented by:

$$\tau_{ij} = \mu \left(\frac{\partial u_i}{\partial x_j} + \frac{\partial u_j}{\partial x_i} - \frac{2}{3} \frac{\partial u_k}{\partial x_k} \delta_{ij} \right), \quad J_j^{\alpha} = -\gamma \frac{\partial \phi_{\alpha}}{\partial x_j}, \quad q_j = -\lambda \frac{\partial T}{\partial x_j}, \quad (3.6)$$

where μ is the fluid dynamic viscosity, T denotes the temperature field, λ is the thermal conductivity and γ is the mass molecular diffusivity coefficient for all of the species. In this formulation we assume using calorically perfect gas in which c_v and c_p , the specific heat at constant volume and constant pressure are constants, and $E = c_v T$ holds. We

assume $\gamma = \mu$ and $\lambda = c_v \gamma$, *i.e.* unity Schmidt number ($Sc = \mu/\gamma = 1$) and Lewis number $Le = \mu c_p/\lambda = c_p/c_v$.

The FDF denoted by F_L , is formally defined as [47]:

$$F_L(\boldsymbol{\psi}, \mathbf{x}, t) = \int_{-\infty}^{+\infty} \rho(\mathbf{x}', t) \zeta(\boldsymbol{\psi}, \boldsymbol{\phi}(\mathbf{x}', t)) G(\mathbf{x}' - \mathbf{x}) d\mathbf{x}', \quad (3.7)$$

where

$$\zeta(\boldsymbol{\psi}, \boldsymbol{\phi}(\mathbf{x}, t)) = \prod_{\alpha=1}^{N_s} \delta(\psi_\alpha - \phi_\alpha(\mathbf{x}, t)). \quad (3.8)$$

In this equation, δ denotes the Dirac delta function, and $\boldsymbol{\psi}$ represents the scalar array in the sample space. The term ζ is the ‘‘fine-grained’’ density [48, 49]. Eq. (3.7) defines FDF as the spatially filtered value of the fine-grained density. With the condition of a positive filter kernel [50], F_L has all the properties of a mass density function [49]. Defining the ‘‘conditional filtered value’’ of $Q(\mathbf{x}, t)$ as

$$\langle Q | \boldsymbol{\psi} \rangle_\ell \equiv \frac{\int_{-\infty}^{+\infty} Q(\mathbf{x}', t) \rho(\mathbf{x}', t) \zeta(\boldsymbol{\psi}, \boldsymbol{\phi}(\mathbf{x}', t)) G(\mathbf{x}' - \mathbf{x}) d\mathbf{x}'}{F_L(\boldsymbol{\psi}, \mathbf{x}, t)}, \quad (3.9)$$

the FDF is governed by the exact transport equation [7]:

$$\begin{aligned} \frac{\partial F_L}{\partial t} + \frac{\partial[\langle u_j(\mathbf{x}, t) | \boldsymbol{\psi} \rangle_\ell F_L]}{\partial x_j} &= -\frac{\partial}{\partial \psi_\alpha} [S_\alpha(\boldsymbol{\psi}) F_L] \\ &+ \frac{\partial}{\partial \psi_\alpha} \left[\left\langle \frac{1}{\rho(\boldsymbol{\phi})} \frac{\partial J_j^\alpha}{\partial x_j} \middle| \boldsymbol{\psi} \right\rangle_\ell F_L \right]. \end{aligned} \quad (3.10)$$

This equation indicates that the effect of chemical reaction (the first term on RHS) appears in a closed form. The unclosed nature of SGS convection and mixing is indicated by the conditional filtered values in the other two terms. For closure of these terms, we use a gradient diffusion model for convection, and the linear mean square estimation (LMSE) model [13, 14] for the molecular mixing. These are given in terms of the stochastic differential equations (SDE’s) [45, 48]:

$$dX_i^+(t) = \left[\langle u_i \rangle_L + \frac{1}{\langle \rho \rangle_\ell} \frac{\partial(\gamma + \gamma_t)}{\partial x_i} \right] dt + \sqrt{2(\gamma + \gamma_t)/\langle \rho \rangle_\ell} dW_i(t), \quad (3.11)$$

$$d\phi_\alpha^+ = -\Omega_m (\phi_\alpha^+ - \langle \phi_\alpha \rangle_L) dt + S_\alpha(\boldsymbol{\phi}^+) dt. \quad (3.12)$$

Here X_i^+ and ϕ_α^+ are probabilistic representations of the position and the scalar variables, respectively. The term dW_i is the Wiener-Levy process [51]. In the model, $\Omega_m = C_\phi (\gamma + \gamma_t) / (\langle \rho \rangle_\ell \Delta^2)$ is the SGS mixing frequency and $C_\phi = 4$ is a model constant. The Fokker-Planck equation corresponding to this model is [52]:

$$\frac{\partial F_L}{\partial t} + \frac{\partial[\langle u_j \rangle_L F_L]}{\partial x_j} = \frac{\partial}{\partial x_j} \left[(\gamma + \gamma_t) \frac{\partial(F_L / \langle \rho \rangle_\ell)}{\partial x_j} \right] + \frac{\partial}{\partial \psi_\alpha} [\Omega_m (\psi_\alpha - \langle \phi_\alpha \rangle_L) F_L] - \frac{\partial[S_\alpha F_L]}{\partial \psi_\alpha}. \quad (3.13)$$

Equation (3.13) represents the modeled FDF transport equation. This equation may be integrated to obtain transport equations for the SGS moments. The equation for the generalized first SGS moment $\langle \phi_\alpha \rangle_L$ and the SGS variance $\tau_\alpha \equiv \tau(\phi_\alpha, \phi_\alpha)$ are:

$$\frac{\partial(\langle \rho \rangle_\ell \langle \phi_\alpha \rangle_L)}{\partial t} + \frac{\partial[\langle \rho \rangle_\ell \langle u_j \rangle_L \langle \phi_\alpha \rangle_L]}{\partial x_j} = \frac{\partial}{\partial x_j} \left[(\gamma + \gamma_t) \frac{\partial(\langle \phi_\alpha \rangle_L)}{\partial x_j} \right] + \langle \rho \rangle_\ell \langle S_\alpha \rangle_L, \quad (3.14)$$

$$\begin{aligned} \frac{\partial(\langle \rho \rangle_\ell \tau_\alpha)}{\partial t} + \frac{\partial[\langle \rho \rangle_\ell \langle u_j \rangle_L \tau_\alpha]}{\partial x_j} = & \frac{\partial}{\partial x_j} \left[(\gamma + \gamma_t) \frac{\partial \tau_\alpha}{\partial x_j} \right] + 2(\gamma + \gamma_t) \left[\frac{\partial(\langle \phi_\alpha \rangle_L)}{\partial x_j} \frac{\partial(\langle \phi_\alpha \rangle_L)}{\partial x_j} \right] \\ & - 2\Omega_m \langle \rho \rangle_\ell \tau_\alpha + 2 \langle \rho \rangle_\ell (\langle \phi_\alpha S_\alpha \rangle_L - \langle \phi_\alpha \rangle_L \langle S_\alpha \rangle_L). \end{aligned} \quad (3.15)$$

These equations are identical to those which would be obtained by employing consistent closures for the SGS fluxes and the dissipation from Eq. (3.4).

Since the FDF is involved only for the scalar variables, all of the hydrodynamic SGS terms need to be modeled by other means. The SGS convected pressure, \mathcal{T}_j , and viscous dissipation, \mathcal{V}_j , are neglected. For SGS convection, the standard Smagorinsky model [53, 54] is used:

$$\begin{aligned} \Sigma_{ij} - \frac{2}{3} \langle \rho \rangle_\ell C_{\nu_2} \Delta^2 S^2 \delta_{ij} = & -2\mu_t \left(\langle S_{ij} \rangle_L - \frac{1}{3} \langle S_{kk} \rangle_L \delta_{ij} \right), \\ M_j^\alpha = & -\gamma_t \frac{\partial \langle \phi_\alpha \rangle_L}{\partial x_j}, \quad \mathcal{E}_j = -c_v \gamma_t \frac{\partial \langle T \rangle_L}{\partial x_j}. \end{aligned} \quad (3.16)$$

Here, S_{ij} is the filtered strain rate tensor $\langle S_{ij} \rangle_L = \frac{1}{2} \left[\frac{\partial \langle u_i \rangle_L}{\partial x_j} + \frac{\partial \langle u_j \rangle_L}{\partial x_i} \right]$. With that, the SGS viscosity is modeled by $\mu_t = \langle \rho \rangle_\ell [C_{\nu_1} \Delta]^2 S$, where $C_{\nu_1} = 0.2$, $C_{\nu_2} = 0.18$, $\gamma_t = \mu_t / Sc_t$, $Sc_t =$

1, $S = \sqrt{2 \langle S_{ij} \rangle_L \langle S_{ij} \rangle_L}$. The parameter Δ denotes the characteristic filter size and is taken as $\Delta = K_p \times (\Delta_x \Delta_y \Delta_z)^{\frac{1}{3}}$, where K_p estimated to be $\frac{1}{2(p+1)}$ with p denoting the polynomial order of approximation of the DG elements.

3.2 RESULTS

To demonstrate its effectiveness, the hybrid DG-MC solver is employed for LES of a three-dimensional, temporally developing mixing layer, as considered in previous DNS [29, 50]. We consider turbulent mixing of two adjacent streams of compressible fluid with different speeds. This flow is considered in the contexts of low, moderate and relatively high compressibility levels. In this configuration, x , y and z denote the stream-wise, the cross-stream and the span-wise flow directions, respectively (Fig. 12). The velocity components in these directions are denoted by u , v and w , respectively. The flow is periodic in the stream-wise and span-wise directions. Both the filtered stream-wise velocity and passive scalar fields are initialised with hyperbolic tangent profiles, where $\langle u \rangle_L = 1$, $\langle \phi \rangle_L = 1$ on the top stream and $\langle u \rangle_L = -1$, $\langle \phi \rangle_L = 0$ on the bottom stream. All of the Reynolds-averaged values are time-dependent and are determined by ensemble averaging over the homogeneous $x - z$ planes. These are denoted by an overbar.

The length L is specified such that $L = 2^{n_p} \lambda_u$, where n_p is the desired number of successive vortex pairings and λ_u is the wavelength of the most unstable mode corresponding to the mean stream-wise velocity profile imposed at the initial time. The flow variables are normalized with respect to the half initial vorticity thickness, $L_r = [\delta_v(t=0)/2]$; $\delta_v = \Delta U / |\partial \overline{u} / \partial y|_{max}$, where \overline{u} is the Reynolds averaged value of the filtered stream-wise velocity and ΔU is the velocity difference across the layer. The reference velocity is $U_r = \Delta U / 2$. The Reynolds number ($Re = \frac{\rho U_r L_r}{\mu}$) is equal to 50 and the Mach number ($Ma = \frac{U_r}{a_r}$) are 0.2, 0.6 and 1.2. Here a_r is the reference speed of sound based on the reference temperature.

Simulations are conducted on a cube box, $0 \leq x \leq L$, $-L/2 \leq y \leq L/2$ and $0 \leq z \leq L$. The 3D field is parametrized in a procedure similar to paper by Vreman *et al.* [50]. The formation of the large scale vortical structures are expedited by harmonic forcing of the

layer. In order to initiate turbulence, both 2D and 3D perturbations are added with a random phase shift between the 3D modes [50, 68, 69]. At low compressibility levels, this results in the formation of two successive vortex pairings and strong three dimensionality caused by growth of secondary instabilities.

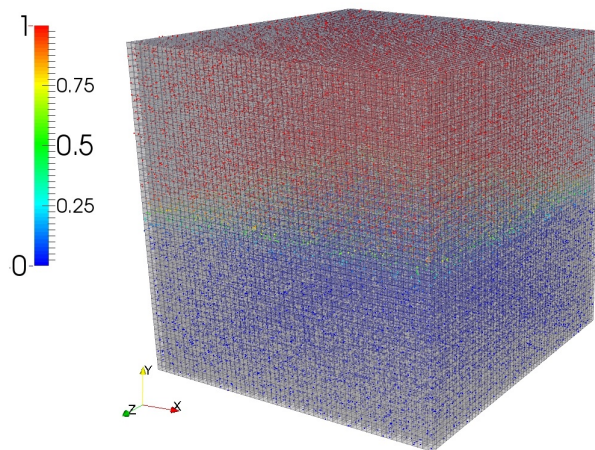


Figure 12: Structured hexahedral mesh and distribution of Monte-Carlo particles within the domain at the initial time. The particles are colored by their scalar values.

The DG-MC FDF simulator is invoked in conjunction with Lax-Friedrichs [57], Roe [58] and artificially upstream flux vector splitting scheme [59] for the advective fluxes, and a symmetric interior penalty method [60, 61] for the diffusive fluxes. Temporal integration in the DG calculations is via a 4th order Runge Kutta method [62]. The SDEs in the MC solver are integrated via the Euler-Marruyamma approximation [9]. The computational domain is discretized on equally spaced cells. These points are used for two purposes: (1) to identify the regions where the statistical information from the MC simulations is obtained; (2) to assess consistency of the coupled DG-MC solver (as described below). Simulations are conducted on a structured hexahedral mesh with a total number of cells equal to 35,937. The MC particles are initially distributed somewhat uniformly throughout the domain. Due to flow periodicity in the stream-wise and span-wise directions, particles that leave the domain at one of these boundaries are replaced by new particles introduced at the opposite boundary

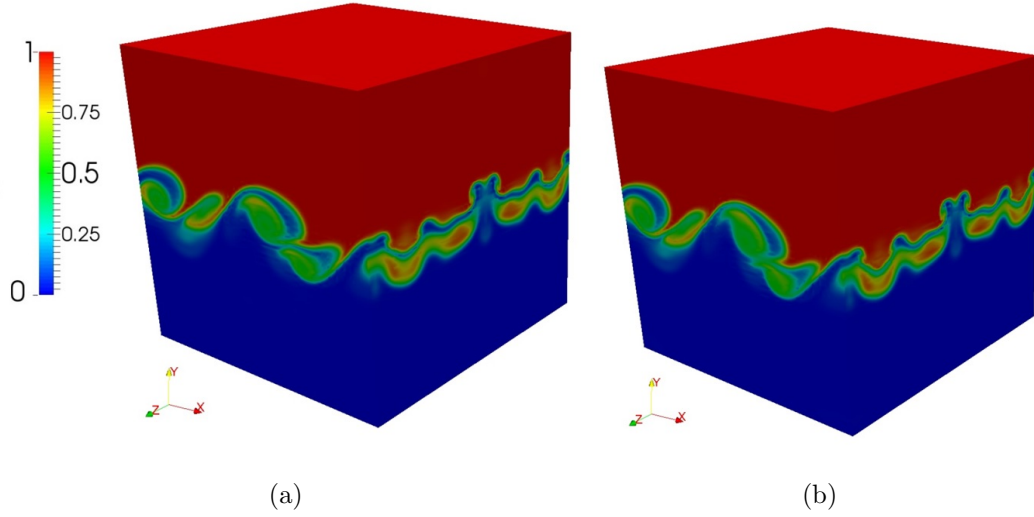


Figure 13: Contour plots of the filtered scalar field for $p = 4$ and $M = 0.2$ at $t = 60$. (a) FDF, (b) DG.

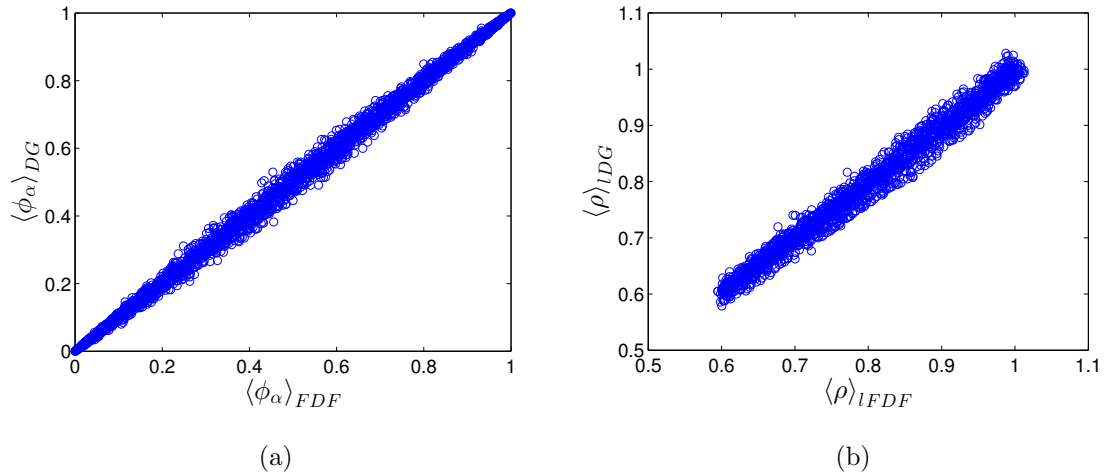


Figure 14: Scatter plot of the filtered values as obtained by FDF vs. those obtained by DG for $p = 4$ and $M = 1.2$ at $t = 80$. (a) filtered scalar, the correlation coefficient is 0.9981. (b) filtered density, the correlation coefficient is 0.9871.

with the same velocity and scalar values. Figure 12 shows the distribution of MC particles inside the cube with the structured mesh at an initial time.

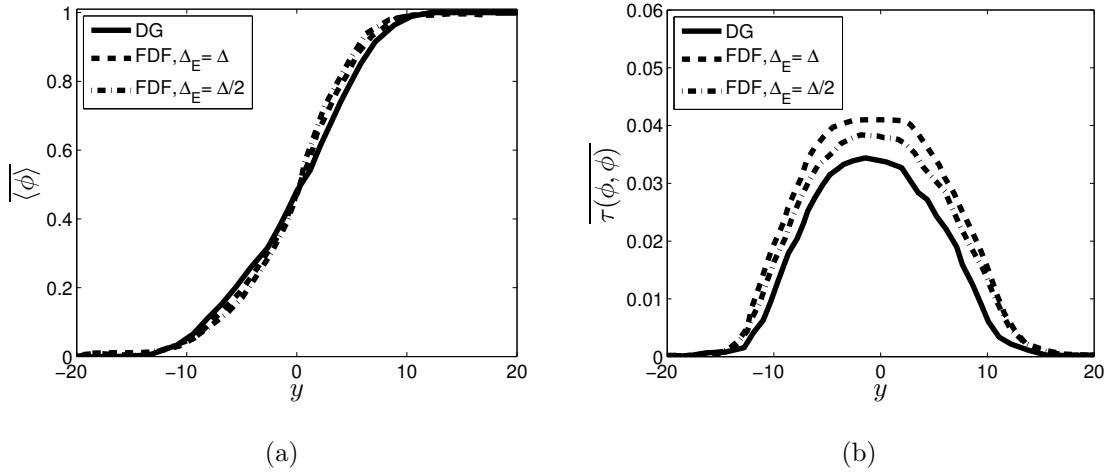


Figure 15: Cross-stream variation of the Reynolds averaged values for $p = 2$, $M = 0.2$ and various ensemble domain size. (a) filtered scalar field, (b) SGS scalar variance.

The simulated results are analyzed both instantaneously and statistically. In the former, the snap-shot contours and scatter plots of the scalar variable are displayed. In the latter, the Reynolds averaged values are considered. In the presentation below, $\tau(a, b) = \langle ab \rangle_L - \langle a \rangle_L \langle b \rangle_L$ denotes the SGS stresses. The resolved stresses are expressed by $R(a, b) = \overline{\langle a \rangle_L \langle b \rangle_L} - \left(\overline{\langle a \rangle_L} \right) \left(\overline{\langle b \rangle_L} \right)$ and the total stresses are given by $r(a, b) = \overline{\langle ab \rangle} - \overline{\langle a \rangle} \overline{\langle b \rangle}$. Note that for a generic filter, $r(a, b) = R(a, b) + \overline{\tau(a, b)}$.

The overall consistency of the simulator is best achieved by comparing the lower moments as obtained from FDF with those simulated directly via DG on the same mesh. Figure 13 shows the instantaneous contour plots of filtered scalar ($\langle \phi_\alpha \rangle_L$) field as computed via both DG and MC. The layer displays strong three-dimensionality, primary vortex roll-up in the span-wise plane, and secondary instabilities in the stream-wise plane. These instabilities are followed by a transition to small-scale turbulence, resulting in a complicated disordered flow, although the roller structures can still be discerned. This figure provides a visual demonstration of the consistency of the FDF simulation as the MC results are in agreement with those via DG. The overall consistency of the conserved scalar and density first moments is further demonstrated in the scatter plots shown in Fig. 14.

A sensitivity analysis is performed to assess the effect of two ensemble sizes on the results. Figure 15 shows the influence of Δ_E in both filtered scalar ($\langle\phi_\alpha\rangle_L$) field and the SGS variance $\overline{\tau(\phi, \phi)}$. It is indicated that, the size of the ensemble domain does not have a significant influence on the Reynolds statistics of the first filtered moments. However, as expected, when the ensemble size is decreased, the FDF results converge to the DG results. The best agreement is observed with a ensemble domain size $\Delta_E = \Delta/2$. Hereinafter, unless otherwise noted, statistics are generated with consideration of $\Delta_E = \Delta/2$.

For $Ma = 0.2$ the most unstable mode is two-dimensional. If the Mach number is higher, the primary instability is three-dimensional. For the supersonic case ($Ma = 1.2$) a pair of opposite oblique modes, becomes most unstable and the primary instability is 3D. For $Ma = 1.2$, shock-waves form on top of the vortices [66, 70–72]. Instantaneous contour plots of the filtered Mach number obtained via the use of $\langle u \rangle_L$ and $\langle T \rangle_L$ displayed in Fig. 16. This figure also shows the ability of both the DG and MC schemes to capture the shocklets. These results are particularly encouraging as they demonstrate that the hybrid DG-MC solver is capable of conducting LES of shock-dominated flows. Figure 17 demonstrates that the filtered density evaluated from the MC particles matches well with that via DG. The particle number density exhibits some oscillations due to statistical errors associated with a finite sample of particles. Figure 18 shows the temporal evolution of the vorticity thickness for different Mach numbers. The growth rate of the most amplified disturbance in the flow is clearly damped with increasing Mach number.

The SGS and the resolved variances for three different Mach numbers are presented in Figs. 19-20. It is observed that the ratio of subgrid scale variance to that resolved is less than 15%. In all cases, the total energy remains somewhat constant, as shown in Fig. 21. For $Ma = 0.2$, the total second moment compared well with DNS results and for $Ma = 0.6$ and 1.2 is consistently calculated via both MC and DG solvers. Consistent with previous DNS results [72], the magnitude of the total stresses decreases as the Mach number increases.

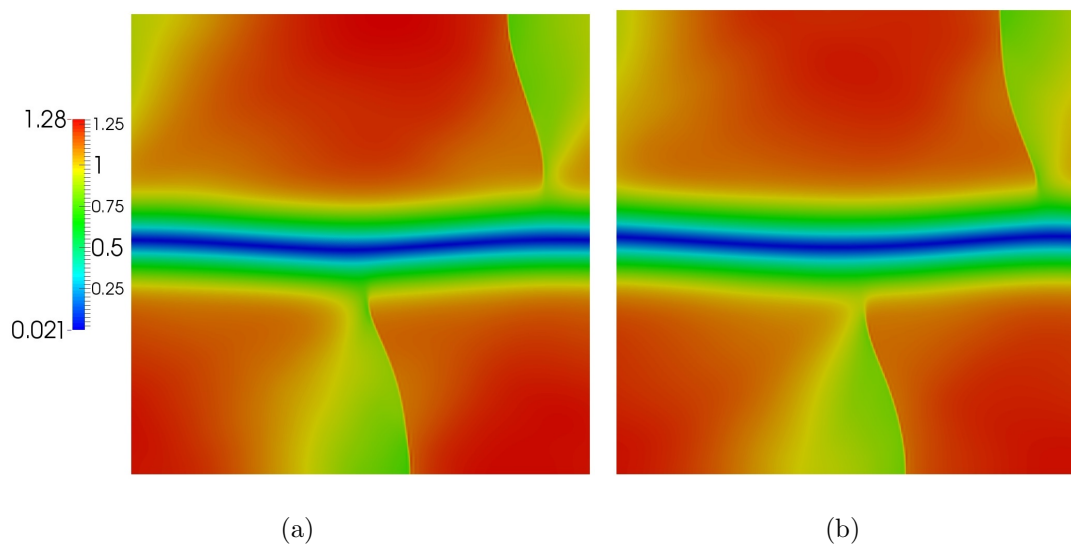
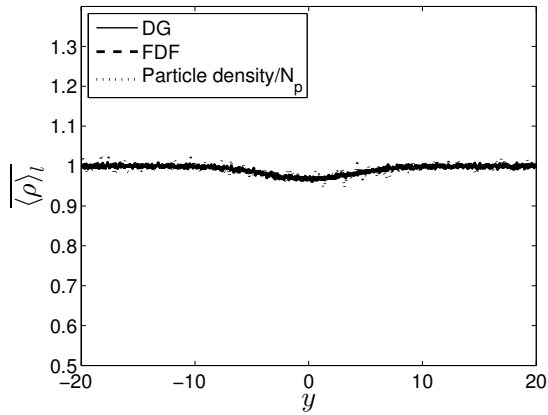
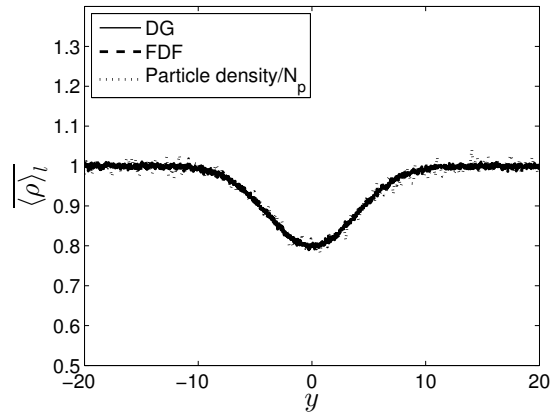


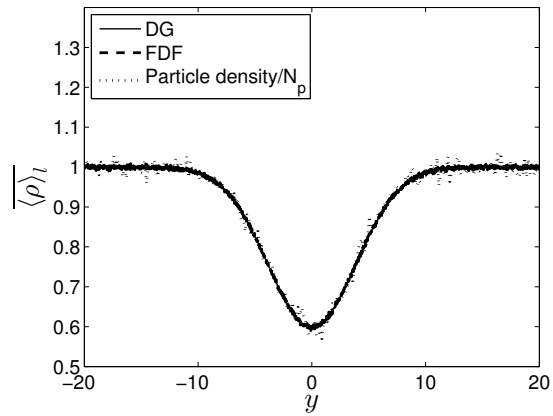
Figure 16: Contour plots of the filtered Mach number for the case with $Ma = 1.2$ at $t = 80$.
(a) FDF, (b) DG.



(a)



(b)



(c)

Figure 17: Cross-stream variation of the filtered density at $t = 80$. (a) $Ma = 0.2$, (b) $Ma = 0.6$ and (c) $Ma = 1.2$.

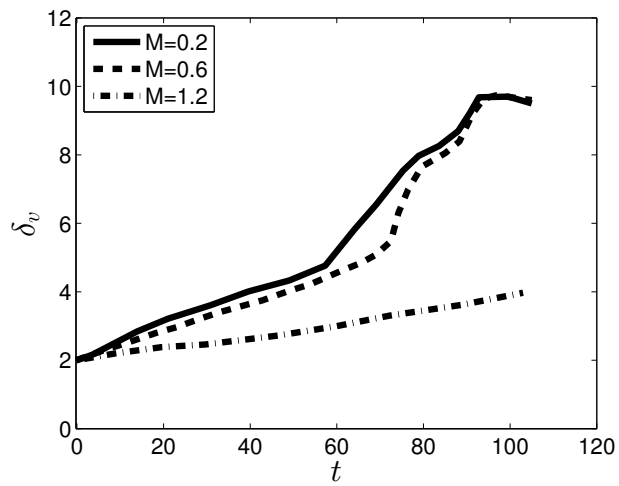


Figure 18: Vorticity thickness vs. time.

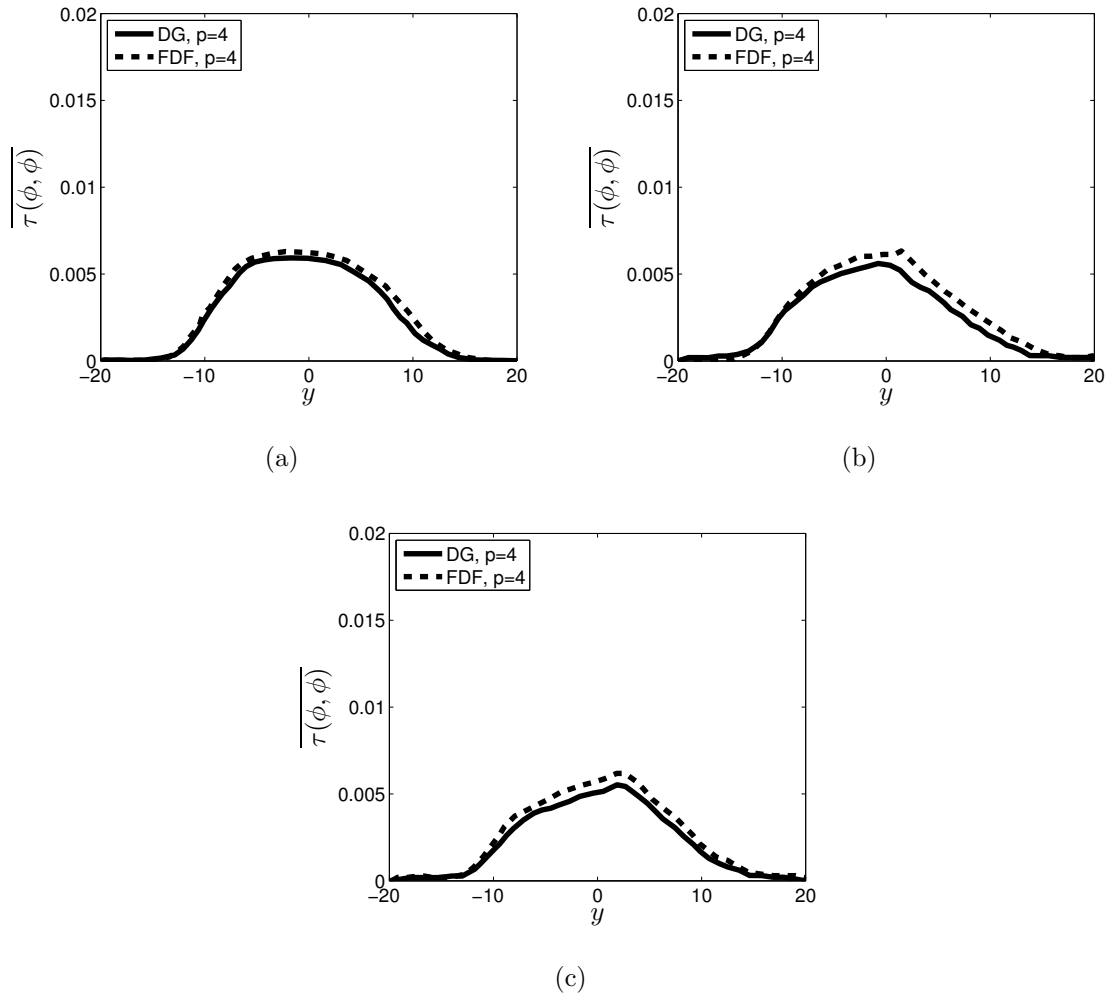


Figure 19: Cross stream variation of the Reynolds averaged SGS scalar variance at $t = 80$.

(a) $Ma = 0.2$, (b) $Ma = 0.6$, (c) $Ma = 1.2$.

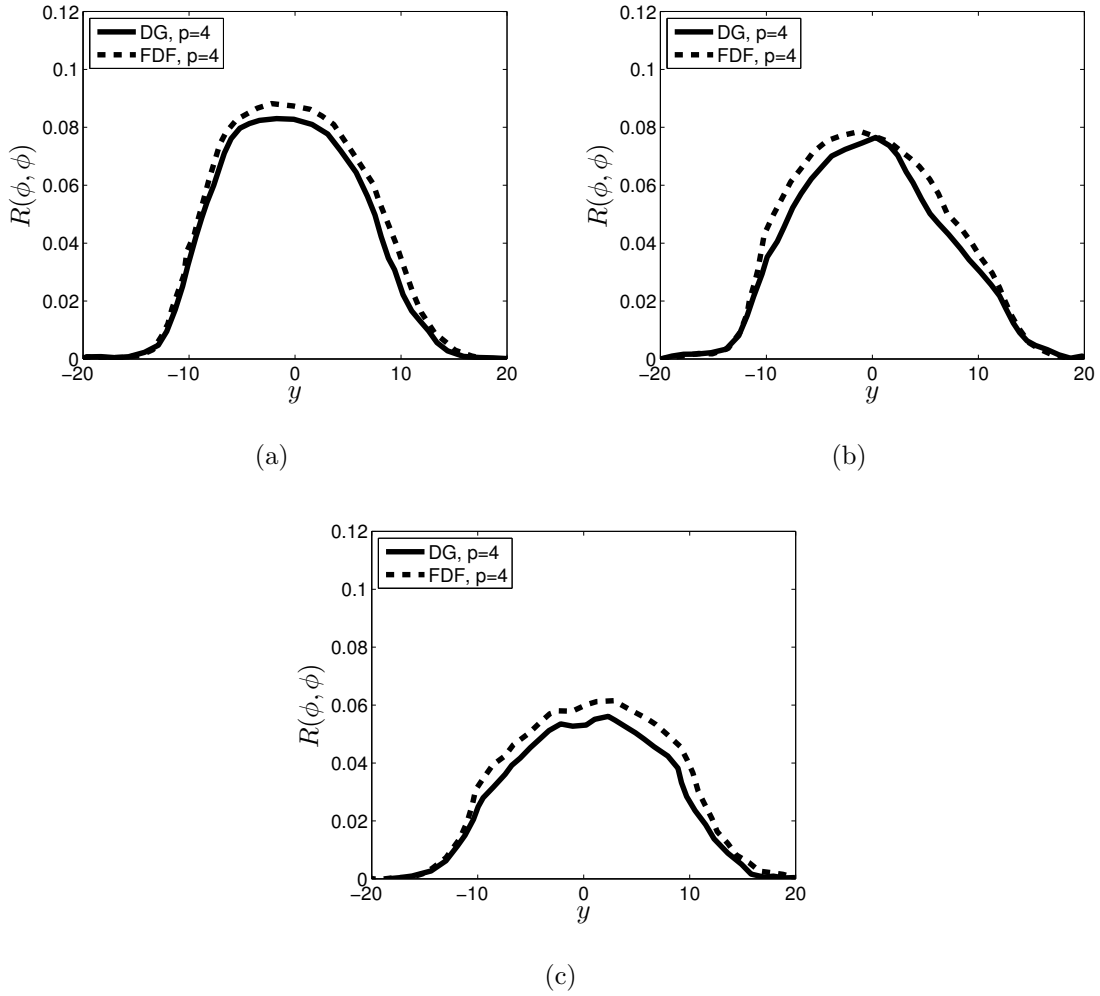


Figure 20: Cross-stream variation of the Reynolds-averaged values of the resolved scalar variance at $t = 80$. (a) $Ma = 0.2$, (b) $Ma = 0.6$, (c) $Ma = 1.2$.

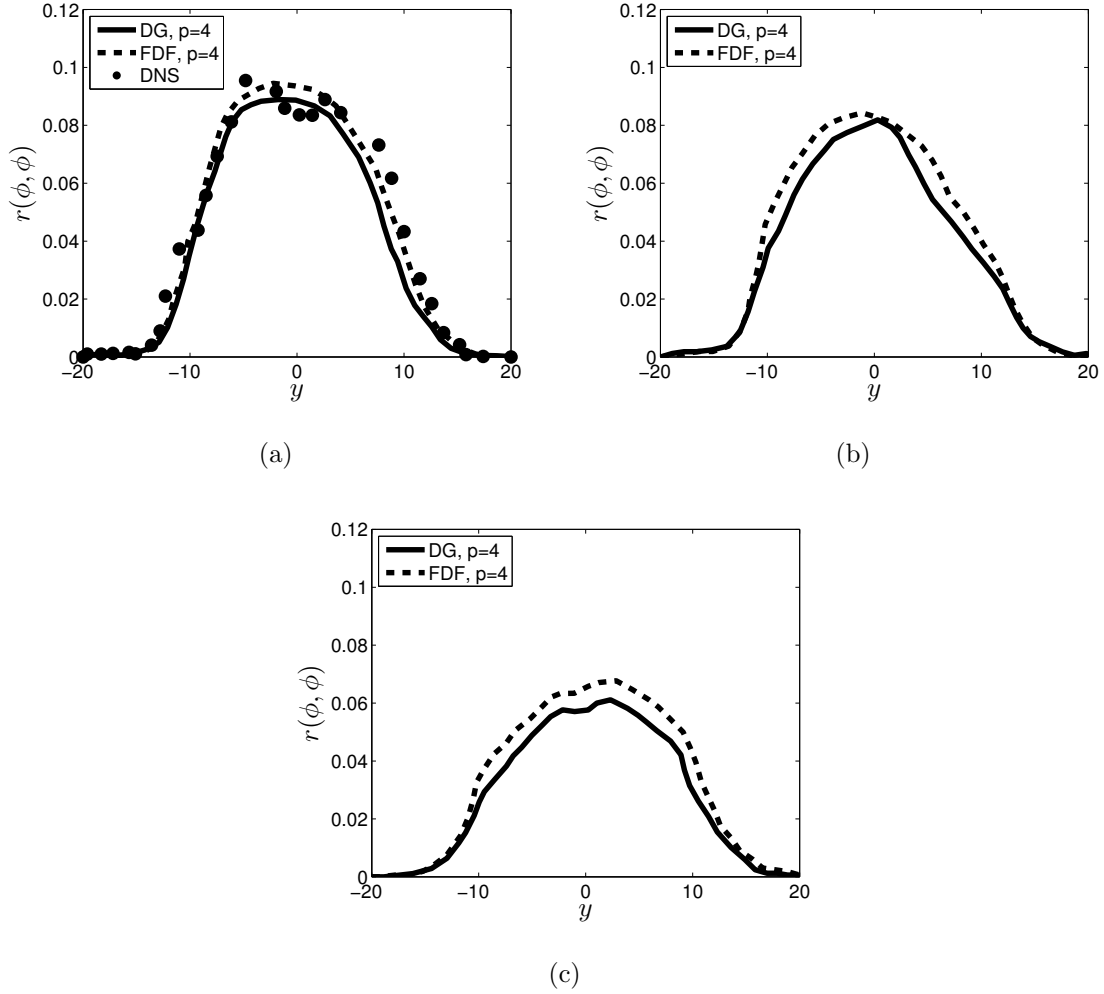


Figure 21: Cross-stream variation of the Reynolds-averaged values of the total scalar variance at $t = 80$. (a) $Ma = 0.2$, (b) $Ma = 0.6$, (c) $Ma = 1.2$.

4.0 CONCLUSION

In this dissertation, the state of the art in turbulent combustion simulation and modeling is advanced. This is done by the merger of a high-order Eulerian discontinuous Galerkin (DG) discretization with a Lagrangian Monte Carlo (MC) solution of the filtered density function (FDF). This merger provide a novel tool for conducting large eddy simulation (LES) of turbulent reacting flows.

In Chapter 2, the methodology is developed and implemented for LES of low speed flows. A three-dimensional temporally developing mixing layer is considered under both non-reacting and reacting conditions. The consistency of the methodology is assessed by comparing the first two moments of the FDF with those obtained by the DG solutions of the same moments' transport equations. The overall predictive capability of the simulator is established via comparisons with previous direct numerical simulation (DNS) data. In Chapter 3, the methodology is extended for LES of high speed compressible flows. In addition to the assessments made in the low speed case, it is shown that the scheme is capable of accurately simulating shock dominated flows.

The properties of the DG-MC simulator can be summarized as follows:

1. The DG method combines the versatility of finite volume discretization with the accuracy of spectral approximations, and is particularly effective when utilized in conjunction with Lagrangian methods.
2. The DG solver supports curved mixed-element meshes, variable discretization order, and non-conforming mesh element refinement. Therefore, it supports combined $h - p$ refinement which results in an optimal solution accuracy for a given computational cost.
3. The DG-MC is capable of conducting accurate LES of shock dominated flows.

4. Even at low p values, when the resolved energy is significantly reduced, the total energy is captured accurately. This feature is particularly attractive when the prediction of the total energies/stresses are of primary concern.
5. The dense kernels of the high-order DG discretization enable superior scalability on massively parallel computer architectures [37]. The solver is designed to scale to very large cases, and simulations involving several billion degrees of freedom are within reach.
6. The superior numerical efficiency and scalability of the DG method can be leveraged by using large polynomial approximation orders $p \sim 4 - 6$. Such large polynomial orders result in very low numerical dissipation [73] which is very desired (in fact essential) in LES.
7. A significant advantage of the proposed methodology is that it will allow us to reach to DNS limit via p -refinement. Based on the close to exponential convergence of this refinement, the procedure is much more efficient than the conventional approach of refining the grid (reducing h) as is the practice in typical Eulerian LES.
8. A particular advantage of the approach is that the DG variables can easily be evaluated at the MC particle locations since these variables are represented by simple polynomials on each element. Hence, there is no loss of accuracy due to the use of a lower order interpolation method as is used in conventional approximations.
9. Due to the high order polynomial approximation, the DG mesh elements are typically much larger than the cells in FD or FV discretizations. This implies that the FDF particles will remain much longer in one element as compared to that in conventional approaches, and thus the computational effort for the particle tracking algorithm will be reduced significantly.

The success of the DG-MC FDF simulator as demonstrated here warrants its further extension and applications for LES of complex turbulent combustion problems.

BIBLIOGRAPHY

- [1] Foster, J. and Miller, R. S., Survey of Turbulent Combustion Models for Large Eddy Simulations of Propulsive Flowfields, in *53rd AIAA Aerospace Sciences Meeting*, Kissimmee, FL, 2015, AIAA, AIAA-2015-1379.
- [2] Pope, S. B., Small Scales, Many Species and the Manifold Challenges of Turbulent Combustion, *Proc. Combust. Inst.*, **34**(1):1 – 31 (2013).
- [3] Kuo, K. K. and Acharya, R., *Fundamentals of Turbulent and Multiphase Combustion*, John Wiley and Sons Inc., Hoboken, NJ, 2012.
- [4] Ansari, N., Jaber, F. A., Sheikhi, M. R. H., and Givi, P., Filtered Density Function as a Modern CFD Tool, in Maher, A. R. S., editor, *Engineering Applications of Computational Fluid Dynamics: Volume 1*, Chapter 1, pp. 1–22, International Energy and Environment Foundation, 2011.
- [5] Almeida, T., Afshari, A., and Jaber, F. A., Modeling and Large-Scale Simulations of Complex Combustion Systems, in Roy, G. D., Yu, K. H., Whitelaw, J. H., and Witton, J. J., editors, *Advances in Combustion and Noise Control*, Chapter 35, pp. 551–564, Cranfield University Press, Cranfield, England, 2006.
- [6] Haworth, D. C. and Pope, S. B., Transported Probability Density Function Methods for Reynolds-Averaged and Large-Eddy Simulations, in Echehki, T. and Mastorakos, E., editors, *Turbulent Combustion Modeling, Fluid Mechanics and Its Applications*, Vol. 95, pp. 119–142, Springer Netherlands, 2011.
- [7] Givi, P., Filtered Density Function for Subgrid Scale Modeling of Turbulent Combustion, *AIAA J.*, **44**(1):16–23 (2006).
- [8] Haworth, D. C., Progress in Probability Density Function Methods for Turbulent Reacting Flows, *Prog. Energ. Combust.*, **36**(2):168–259 (2010).
- [9] Kloeden, P. E., Platen, E., and Schurz, H., *Numerical Solution of Stochastic Differential Equations through Computer Experiments*, Springer, Berlin; New York, second edition, 1997.

- [10] Grigoriu, M., *Applied Non-Gaussian Processes*, Prentice-Hall, Englewood Cliffs, NJ, 1995.
- [11] Madnia, C. K., Jaber, F. A., and Givi, P., Large Eddy Simulation of Heat and Mass Transport in Turbulent Flows, in Minkowycz, W. J., Sparrow, E. M., and Murthy, J. Y., editors, *Handbook of Numerical Heat Transfer*, Chapter 5, pp. 167–189, John Wiley & Sons, Inc., Hoboken, NJ, second edition, 2000.
- [12] Ansari, N., Goldin, G. M., Sheikhi, M. R. H., and Givi, P., Filtered Density Function Simulator on Unstructured Meshes, *J. Comput. Phys.*, **230**(19):7132–7150 (2011).
- [13] Colucci, P. J., Jaber, F. A., Givi, P., and Pope, S. B., Filtered Density Function for Large Eddy Simulation of Turbulent Reacting Flows, *Phys. Fluids*, **10**(2):499–515 (1998).
- [14] Jaber, F. A., Colucci, P. J., James, S., Givi, P., and Pope, S. B., Filtered Mass Density Function for Large-Eddy Simulation of Turbulent Reacting Flows, *J. Fluid Mech.*, **401**:85–121 (1999).
- [15] Garrick, S. C., Jaber, F. A., and Givi, P., Large Eddy Simulation of Scalar Transport in a Turbulent Jet Flow, in Knight, D. and Sakell, L., editors, *Recent Advances in DNS and LES, Fluid Mechanics and its Applications*, Vol. 54, pp. 155–166, Springer Netherlands, 1999.
- [16] Raman, V., Pitsch, H., and Fox, R. O., Hybrid Large-Eddy Simulation/Lagrangian Filtered-Density-Function Approach for Simulating Turbulent Combustion, *Combust. Flame*, **143**(1–2):56–78 (2005).
- [17] Drozda, T. G., Sheikhi, M. R. H., Madnia, C. K., and Givi, P., Developments in Formulation and Application of the Filtered Density Function, *Flow Turbul. Combust.*, **78**(1):35–67 (2007).
- [18] Yilmaz, S. L., Nik, M. B., Givi, P., and Strakey, P. A., Scalar Filtered Density Function for Large Eddy Simulation of a Bunsen Burner, *J. Propul. Power*, **26**(1):84–93 (2010).
- [19] Drozda, T. G., Quinlan, J. R., Piscuineri, P. H., and Yilmaz, S. L., Progress Toward Affordable High Fidelity Combustion Simulations for High-Speed Flows in Complex Geometries, in *48th AIAA/ASME/SAE/ASEE Joint Propulsion Conference & Exhibit*, pp. 1–16, Atlanta, GA, 2012, AIAA, AIAA-2012-4264.
- [20] Banaeizadeh, A., Li, Z., and Jaber, F. A., Compressible Scalar Filtered Density Function Model for High-Speed Turbulent Flows, *AIAA J.*, **49**(10):2130–2143 (2011).
- [21] Ansari, N., Piscuineri, P. H., Strakey, P. A., and Givi, P., Scalar-Filtered Mass-Density-Function Simulation of Swirling Reacting Flows on Unstructured Grids, *AIAA J.*, **50**(11):2476–2482 (2012).

- [22] Afshari, A., Jaberri, F., and Shih, T., Large-Eddy Simulations of Turbulent Flows in an Axisymmetric Dump Combustor, *AIAA J.*, **46**(7):1576–1592 (2008).
- [23] Ansari, N., Strakey, P. A., Goldin, G., and Givi, P., Filtered Density Function Simulation of a Realistic Swirled Combustor, *Proc. Combust. Inst.*, **35**(2):1433–1442 (2015).
- [24] Esmaelli, M., Afshari, A., and Jaberri, F. A., Turbulent Mixing in Non-Isothermal Jet in Cross-Flow, *Int. J. Heat Mass. Tran.*, **89**:1239–1257 (2015).
- [25] Tirunagari, R. R. and Pope, S. B., LES/PDF for Premixed Combustion in the DNS Limit, *Combust. Theor. Model.*, **20**(5):834–865 (2016).
- [26] Gheimassi, A. N., Givi, P., Nik, M. B., and Pope, S. B., Pressure-Velocity-Scalar Filtered Mass Density Function for Large Eddy Simulation of Compressible Turbulent Flow, in *Bulletin of the American Physical Society, 68th Annual Meeting of the APS Division of Fluid Dynamics*, Vol. 60, p. 565, Boston, MA, 2015, American Physical Society.
- [27] Heinz, S., *Statistical Mechanics of Turbulent Flows*, Springer-Verlag, New York, NY, 2003.
- [28] Sheikhi, M. R. H., Drozda, T. G., Givi, P., and Pope, S. B., Velocity-Scalar Filtered Density Function for Large Eddy Simulation of Turbulent Flows, *Phys. Fluids*, **15**(8):2321–2337 (2003).
- [29] Sheikhi, M. R. H., Givi, P., and Pope, S. B., Velocity-Scalar Filtered Mass Density Function for Large Eddy Simulation of Turbulent Reacting Flows, *Phys. Fluids*, **19**(9):095106 (2007).
- [30] Sheikhi, M. R. H., Givi, P., and Pope, S. B., Frequency-Velocity-Scalar Filtered Mass Density Function for Large Eddy Simulation of Turbulent Flows, *Phys. Fluids*, **21**(7):075102 (2009).
- [31] Nik, M. B., Yilmaz, S. L., Givi, P., Sheikhi, M. R. H., and Pope, S. B., Simulation of Sandia Flame D using Velocity-Scalar Filtered Density Function, *AIAA J.*, **48**(7):1513–1522 (2010).
- [32] Yilmaz, S. L., Ansari, N., Piscuneri, P. H., Nik, M. B., Otis, C. C., and Givi, P., Advances in FDF Modeling and Simulation, in *47th AIAA/ASME/SAE/ASEE Joint Propulsion Conference & Exhibit*, pp. 1–11, San Diego, CA, 2011, AIAA, AIAA-2011-5918.
- [33] Sheikhi, M. R. H., Safari, M., and Hadi, F., Entropy Filtered Density Function for Large Eddy Simulation of Turbulent Flows, *AIAA J.*, **53**(9):2571–2587 (2015).
- [34] Yilmaz, S. L., Nik, M. B., Sheikhi, M. R. H., Strakey, P. A., and Givi, P., An Irregularly Portioned Lagrangian Monte Carlo Method for Turbulent Flow Simulation, *J. Sci. Comput.*, **47**(1):109–125 (2011).

- [35] Pisciueneri, P. H., Yilmaz, S. L., Strakey, P. A., and Givi, P., An Irregularly Portioned FDF Simulator, *SIAM J. Sci. Comput.*, **35**(4):C438–C452 (2013).
- [36] Pisciueneri, P. H., Yilmaz, S. L., Strakey, P. A., and Givi, P., Massively Parallel FDF Simulation of Turbulent Reacting Flows, in Heinz, S. and Bessaih, H., editors, *Stochastic Equations for Complex Systems: Theoretical and Computational Topics*, Mathematical Engineering, Chapter 8, Springer, 2015.
- [37] Brazell, M. and Mavriplis, D. J., 3D Mixed Element Discontinuous Galerkin with Shock Capturing, in *21st AIAA CFD Conference*, San Diego, CA, 2013, AIAA, AIAA-2013-2855.
- [38] Wang, L. and Mavriplis, D. J., Adjoint Based h-p Adaptive Discontinuous Galerkin Methods for Aerospace Applications, in *AIAA Aerospace Sciences Meeting*, Orlando, FL, 2009, AIAA, AIAA-2009-0952.
- [39] Sammak, S., Ansari, N., Givi, P., Brazell, M. J., and Mavriplis, D. J., A DG-FDF Large Eddy Simulator, in *Bulletin of the American Physical Society, 67th Annual Meeting of the APS Division of Fluid Dynamics*, Vol. 59, p. 496, San Francisco, CA, 2014, American Physical Society.
- [40] Sammak, S., Givi, P., Brazell, M. J., and Mavriplis, D. J., A Coupled DG-MC Method for FDF Simulation, in *International Conference on Model Integration across Disparate Scales in Complex Turbulent Flow Simulation*, State College, PA, 2015.
- [41] Sammak, S., Brazell, M. J., Givi, P., and Mavriplis, D. J., A Hybrid DG-Monte Carlo FDF Simulator, *Comput. Fluids*, **140**(13):158–166 (2016).
- [42] Sammak, S., Brazell, M. J., Mavriplis, D. J., and Givi, P., Discontinuous Galerkin-Monte Carlo Solver for Large Eddy Simulation of Compressible Turbulent Flows, in *AIAA Aerospace Sciences Meeting*, Grapevine, TX, 2017, AIAA, in press.
- [43] Sammak, S., Brazell, M. J., Mavriplis, D. J., and Givi, P., DG-FDF Solver for Large Eddy Simulation of Compressible Flows, in *Bulletin of the American Physical Society, 69th Annual Meeting of the APS Division of Fluid Dynamics*, Vol. 61, p. 599, Portland, OR, 2016, American Physical Society.
- [44] Sammak, S., Nouri, A. G., Ansari, N., and Givi, P., Quantum Computing and Its Potential for Turbulence Simulations, in Danaev, N., Shokin, Y., and Akhmed-Zakin, D., editors, *Mathematical Modeling of Technological Processes*, Communications in Computer and Information Science, Chapter 13, pp. 124–132, Springer, 2015.
- [45] Pope, S. B., *Turbulent Flows*, Cambridge University Press, Cambridge, U.K., 2000.
- [46] Piomelli, U., Large-Eddy Simulation: Achievements and Challenges, *Prog. Aerosp. Sci.*, **35**(4):335–362 (1999).

- [47] Pope, S. B., Computations of Turbulent Combustion: Progress and Challenges, *Proc. Combust. Inst.*, **23**(1):591–612 (1990).
- [48] O’Brien, E. E., The Probability Density Function (PDF) Approach to Reacting Turbulent Flows, in Libby, P. and Williams, F., editors, *Turbulent Reacting Flows, Topics in Applied Physics*, Vol. 44, Chapter 5, pp. 185–218, Springer, Heidelberg, 1980.
- [49] Pope, S. B., PDF Methods for Turbulent Reactive Flows, *Prog. Energ. Combust.*, **11**(2):119–192 (1985).
- [50] Vreman, B., Geurts, B., and Kuerten, H., Realizability Conditions for the Turbulent Stress Tensor in Large-Eddy Simulation, *J. Fluid Mech.*, **278**:351–362 (1994).
- [51] Gikhman, I. I. and Skorokhod, A. V., *Stochastic Differential Equations*, Springer-Verlag, New York, NY, 1972.
- [52] Risken, H., *The Fokker-Planck Equation, Methods of Solution and Applications*, Springer-Verlag, New York, NY, 1989.
- [53] Smagorinsky, J., General Circulation Experiments with the Primitive Equations. I. The Basic Experiment, *Mon. Weather Rev.*, **91**(3):99–164 (1963).
- [54] Ghosal, S. and Moin, P., The Basic Equations for the Large Eddy Simulation of Turbulent Flows in Complex Geometry, *J. Comput. Phys.*, **118**(1):24–37 (1995).
- [55] Givi, P. and Madnia, C. K., Spectral Methods in Combustion, in Chung, T. J., editor, *Numerical Modeling in Combustion*, Chapter 8, pp. 409–452, Taylor & Francis, Washington, D.C., 1993.
- [56] Subramaniam, S. and Haworth, D. C., A Probability Density Function Method for Turbulent Mixing and Combustion on Three-Dimensional Unstructured Deforming Meshes, *Int. J. Engine Res.*, **1**(2):171–190 (2000).
- [57] Lax, P. D., Weak Solutions of Nonlinear Hyperbolic Equations and Their Numerical Computation, *Comm. Pure Appl. Math.*, **7**(1):159–193 (1954).
- [58] Roe, P. L., Approximate Riemann Solvers, Parameter Vectors and Difference Schemes, *J. Comput. Phys.*, **43**(2):357–372 (1981).
- [59] Sun, M. and Takayama, K., An Artificially Upstream Flux Vector Splitting Scheme for the Euler Equations, *J. Comput. Phys.*, **189**(1):305–329 (2003).
- [60] Shahbazi, K., Mavripllis, D. J., and Burgess, N. K., Multigrid Algorithms for High-order Discontinuous Galerkin Discretizations of the Compressible Navier-Stokes Equations, *J. Comput. Phys.*, **228**(21):7917–7940 (2009).

- [61] Hartmann, R. and Houston, P., An Optimal Order Interior Penalty Discontinuous Galerkin Discretization of the Compressible Navier-Stokes Equations, *J. Comput. Phys.*, **227**(22):9670–9685 (2008).
- [62] Jameson, A., Schmidt, W., and Turkel, E., Numerical Solution of the Euler Equations by Finite Volume Methods Using Runge Kutta Time Stepping Schemes, in *14th AIAA Fluid and Plasma Dynamics Conference*, Palo Alto, CA, 1981, AIAA, AIAA-1981-1259.
- [63] Bilger, R. W., Future Progress in Turbulent Combustion Research, *Prog. Energ. Combust.*, **26**(4–6):367–380 (2000).
- [64] Poinso, T. and Veynante, D., *Theoretical and Numerical Combustion*, R. T. Edwards, Inc., Philadelphia, PA, second edition, 2005.
- [65] Williams, F. A., *Combustion Theory*, The Benjamin/Cummings Publishing Company, Menlo Park, CA, second edition, 1985.
- [66] Garnier, E., Adams, N., and Sagaut, P., *Large Eddy Simulation for Compressible Flows*, Springer, New York, NY, 2009.
- [67] Sagaut, P., *Large Eddy Simulation for Incompressible Flows*, Springer, New York, NY, third edition, 2010.
- [68] Moser, R. D. and Rogers, M. M., The Three-Dimensional Evolution of a Plane Mixing Layer: Pairing and Transition to Turbulence, *J. Fluid Mech.*, **247**:275–320 (1993).
- [69] Sandham, N. D. and Reynolds, W. C., Three-Dimensional Simulations of Large Eddies in the Compressible Mixing Layer, *J. Fluid Mech.*, **224**:133–158 (1991).
- [70] Sandham, N. D. and Reynolds, W. C., Some Inlet-Plane Effects on the Numerically Simulated Spatially-Developing Mixing Layer, in *Turbulent Shear Flows 6*, pp. 441–454, Springer, 1989.
- [71] Miller, R. S., Madnia, C. K., and Givi, P., Structure of a Turbulent Reacting Mixing Layer, *Combust. Sci. Technol.*, **99**:1–36 (1994).
- [72] Givi, P., Madnia, C. K., Steinberger, C. J., Carpenter, M. H., and Drummond, J. P., Effects of Compressibility and Heat Release in a High Speed Reacting Mixing Layer, *Combust. Sci. Technol.*, **78**(1-3):33–67 (1991).
- [73] Gassner, G. J. and Beck, A. D., On the Accuracy of High-order Discretizations for Underresolved Turbulence Simulations, *Theor. Comp. Fluid. Dyn.*, **27**(3-4):221–237 (2013).